

Floquet-Weyl semimetals generated by an optically resonant interband-transition

Runnan Zhang,¹ Ken-ichi Hino,^{2,3,*} and Nobuya Maeshima^{3,2}

¹*Doctoral Program in Materials Science, Graduate School of Pure and Applied Sciences,
University of Tsukuba, Tsukuba, Ibaraki 305-8573, Japan*

²*Division of Materials Science, Faculty of Pure and Applied Sciences,
University of Tsukuba, Tsukuba 305-8573, Japan*

³*Center for Computational Sciences, University of Tsukuba, Tsukuba 305-8577, Japan*

(Dated: May 26, 2022)

Floquet-Weyl semimetals (FWSMs) generated by irradiation of a continuous-wave laser with left-hand *circular* polarization (rotating in counterclockwise sense with time) on the group II-V narrow gap semiconductor Zn_3As_2 are theoretically investigated, where the frequency of the laser is set nearly *resonant* with a band gap of the crystal. It is found that the excitation of the crystal by such a laser induce two types of FWSM phases that differ absolutely in characters. To be specific, the associated two pairs of Weyl points are stably formed by band touching between Floquet sidebands ascribable to a valence band labeled as $J_z = \pm 3/2$ and a conduction band labeled as $J_z = \pm 1/2$, where J_z represents the z -component of total angular momentum quantum number of Γ -point and a double sign corresponds. Here, one FWSM state composed of the up-spin Floquet sidebands relevant to $J_z = 3/2$ and $1/2$ shows almost quadratic band-touching in the vicinity of the associated pair of Weyl points, while the other FWSM state composed of the down-spin Floquet sidebands relevant to $J_z = -3/2$ and $-1/2$ shows linear band-touching. Further, it is revealed that both up-spin and down-spin sidebands host nontrivial two-dimensional surface states that are pinned to the respective pairs of the Weyl points. Both surface states also show different energy dispersions and physical properties. More detailed discussion is made in the text on the origin of the above findings, chirality of the FWSM phases, alteration of topological order, laser-induced magnetic properties, and so on.

I. INTRODUCTION

Topological materials have been studied for more than a decade¹⁻⁴ and growing interest has been directed toward the exploration of a class of topological semimetals (SMs)⁵⁻²¹ — such as Weyl SMs (WSMs), Dirac SMs (DSMs), and nodal-line SMs (NLSMs) — in addition with further deepening of the studies of prototypical topological insulators, for instance, on non-Hermitian topological systems,^{22,23} topological photonics,²⁴ higher-order topological insulators,²⁵⁻²⁷ topological excitons,²⁸⁻³⁰ topological surface plasmon polaritons,^{31,32} and so on. WSMs and DSMs are three dimensional (3D) gapless phases of materials, in which bands cross linearly at points protected by topology and symmetry. There is close connection with the chiral anomaly (the Adler-Bell-Jackiw anomaly) in linearly dispersing fermionic excitations in particle physics, which gives rise to the nonconservation of an axial current even for a massless particle.³³⁻³⁹ In accord with the prediction of the chiral anomaly, large negative magnetic resistance is observed in magnetotransport in WSMs.⁴⁰⁻⁴³ Further, these SMs exhibit a great number of novel transport properties such as ultra-high mobility, titanic magnetic resistance, and anomalous Hall conductivity.^{8,17,40,44-51} In NLSMs, bands cross along special lines in the Brillouin zone (BZ) in the shape of a closed ring or a line. Breaking of either time-reversal (T-) symmetry or spatial-inversion (I-) symmetry leads DSMs and NLSMs to WSMs.¹⁹ In the T-breaking WSMs, there are a pair of Weyl nodes with opposite chirality, on which a surface state is pinned with a characteristic Fermi arc, while the

number of Weyl nodes in the I-breaking WSMs is a multiple of four.^{6,18}

An interaction of topological SMs with a continuous-wave laser provides the studies of topological materials with another avenue from the perspective of the quantum control of underlying topological properties by means of built-in laser parameters — intensity, frequency ω , and polarization — and the exploration of topological phases that are in non-equilibrium.⁵²⁻⁷¹ Here, the total Hamiltonian $H(t)$ of concern at time t has temporal periodicity $H(t) = H(t + T)$ to ensure the Floquet theorem with $T = 2\pi/\omega$.⁷² By the drive with a circularly polarized laser — in place of the application of a static intrinsic Zeeman field —, the T-symmetry in DSMs and NLSMs is broken to form WSMs, and these are termed as Floquet WSMs (FWSMs). This scenario for creating FWSMs is applied to the DSMs of alkali pnictides NaBi_3 ,⁵⁵ type-II and hybrid LNSMs,⁵⁸ and 3D stacked graphene systems.⁵⁶ In particular, it is reported that the drive of a 3D Luttinger semimetal by an elliptically polarized light leads to the coexistence of WSM phases with double and single Weyl points, which can be tuned to be type-I or type-II.⁶⁹ Further, by virtue of Floquet engineering due to periodical driving of hybrid multi-WSM phases, the number of various isolated band touching points can be increased on-demand by tuning system parameters, where intricate Fermi arc structures are hosted.⁷⁰ In addition, NLSMs are driven to result in FWSMs, revealing a photovoltaic anomalous Hall effect associated with the Weyl point nodes.⁵⁴ Very recently, frequency-independent magnetization mechanisms in response to circularly polarized light are studied in WSMs.^{62,64}

As regards the I-symmetry, this is also broken by the introduction of an interaction of electron with the continuous-wave laser. However, the time-glide I-symmetry holds correct instead to realize the same invariance in $H(t)$ as the I-symmetry.^{65,73} The symmetry operation associated with this symmetry is represented by the operation of putting time t ahead by a half period $T/2$, followed by the I-operation.

In most of theoretical studies of Floquet topological materials,^{74–83} an electron-light interaction is introduced exclusively by employing the Peierls phase transform — given by the replacement of a Bloch momentum \mathbf{k} by $\mathbf{k} + \mathbf{A}(t)$ — under the off-resonant condition that $\omega \gg E_g$. Here, $\mathbf{A}(t)$ and E_g represent a vector potential of the laser at t , and a bandgap of the concerned material, respectively, and the atomic units are used. Further, the effective Floquet Hamiltonian is constructed by relying on the Floquet-Magnus expansion with respect to E_g/ω .^{84–86} It is remarked that the convergence of this expansion is not ensured at the resonant limit of $\omega = E_g$.⁸⁶ The resulting Floquet bands are likely modified from original bands before laser irradiation. It is assumed that under the above off-resonant condition, effects of interband electric-dipole transitions between a valence band and a conduction band are negligibly small, compared with those of the above-mentioned Peierls interaction.^{52,55,82} Here, interband and intraband couplings caused by the electron-light interaction due to the Peierls phase transform are termed as the Peierls interaction to make a distinction from the interband electric-dipole interaction.

The aim of this paper is to create a FWSM phase by driving Zn_3As_2 ^{87–90} belonging to the group II-V semiconductors with a circularly polarized laser which meets an almost on-resonant condition $\omega \approx E_g$,^{65,77} and to explore the properties of surface states hosted by this FWSM. It is remarked that this material is topologically trivial without band inversion. This differs from a DSM of Cd_3As_2 ,^{87,89,91–93} realized by the band-inversion mechanism due to the presence of a $n(> 2)$ -fold uniaxial rotational symmetry along a symmetry line, hosting edge modes known as double Fermi arcs at the surfaces.^{7,8,11,14,18} The creation of the FWSM is governed by an almost resonant transition due to the interband electric-dipole interaction rather than that due to the Peierls interaction, as shown in more detail later (Sec. III). This is the key issue of this paper.

Below, a more detailed explanation is made on this key issue based on the four-band model of the semiconductor Zn_3As_2 , where the valence and conduction bands are labeled as $J_z = \pm 3/2$ and $\pm 1/2$, respectively, with J_z as the z -component of total angular momentum quantum number at the Γ -point ($\mathbf{k} = \mathbf{0}$). First, given the driving laser with a left-hand circular polarization (rotating in counterclockwise sense with time), the coupling of this light with an electric dipole moment induced by the transition between the down-spin bands with $J_z = -3/2$ and $-1/2$ is dominant over that between the up-spin bands

with $J_z = 3/2$ and $1/2$.⁹⁴ This is maximized when the on-resonant condition is met. It is remarked that the roles of the up-spin and down-spin bands are exchanged for a laser with a right-hand circular polarization. A left-hand polarization is favored throughout this paper unless otherwise stated. Second, as the laser intensity increases, the ac-Stark effect gives rise to larger energy splitting of each down-spin band into two leaves with conspicuous modification of the band profile,^{65,95–97} whereas the up-spin bands are just slightly affected. The ac-Stark effect is also maximized by the on-resonant condition. Third, the present resonant interband-transition yields real carrier excitation, differing from virtual carrier excitation due to the off-resonant one. Thus, it is likely that orbital magnetization results from the inverse Faraday effect that is a non-linear optical process caused by a circularly polarized laser field.^{62–64,66,98–102} Consequently, it is expected that the laser drive with a circular polarization in the almost on-resonant condition provides intriguing physics with FWSMs, which is sharply distinct from the conventional off-resonant laser drive.^{52,55,82}

The remainder of this paper is organized as follows. Section II describes the theoretical framework, Sec. III presents the results and discussion, and Sec. IV presents the conclusion. Further, three appendices are included. Hereafter, the atomic units (a.u.) are used throughout, unless otherwise stated.

II. THEORY

A. Effective Hamiltonian

The crystal of concern, Zn_3As_2 , is a narrow gap semiconductor, the structure of which is very similar to that of Cd_3As_2 , though in the latter, a band is inverted to result in a DSM.^{87,89,91–93} There are many equilibrium phases of Zn_3As_2 depending on pressure and temperature, for instance, $\alpha\text{Zn}_3\text{As}_2$ (with a body-centered tetragonal structure $I4_1/cd$) and $\alpha'\text{Zn}_3\text{As}_2$ (with a tetragonal structure $P4_2/nbc$).⁸⁸ Here, one employs the structure of $\alpha'\text{Zn}_3\text{As}_2$ having the C_4 -rotational symmetry along the Γ - Z axis in the BZ for constructing an effective Hamiltonian. The low-energy electronic properties of it are mostly determined by the conduction band composed of Zn $4s$ -orbitals and the valence band composed of As $4p$ -orbitals.

Here, an effective electronic Hamiltonian for Zn_3As_2 is constructed by following the Kane model used in Ref. 8 for the crystal structure of Cd_3As_2 with a tetragonal structure $P4_2/nbc$. To be specific, one considers the following four states as conduction s -states $|\Gamma_6, J_z = \pm 1/2\rangle$ and heavy-hole p -states $|\Gamma_7, J_z = \pm 3/2\rangle$, and light-hole states and split-off states are disregarded because of relatively large energy separation from these four states at the Γ -point. The effective Hamiltonian is read as the

4 × 4-matrix:^{103,104}

$$\mathcal{H}(\mathbf{k}) = c(\mathbf{k})I + \sum_{j=3}^5 d_j(\mathbf{k})\gamma_j \quad (1)$$

with $\mathbf{k} = (k_x, k_y, k_z)$ as a 3D Bloch momentum. Here, γ_j 's represent the four-dimensional Dirac matrices for the Clifford algebra, defined by $\gamma_1 = \tau_x \otimes \sigma_x$, $\gamma_2 = \tau_x \otimes \sigma_y$, $\gamma_3 = \tau_x \otimes \sigma_z$, $\gamma_4 = \tau_z \otimes I_2$, and $\gamma_5 = \tau_y \otimes I_2$, where I and I_2 represent the 4×4 and 2×2 unit matrices, respectively, τ_l and σ_l with $l = x, y, z$ represent the Pauli matrices for orbital and spin degrees of freedom, respectively, and the anti-commutation relation, $\{\gamma_j, \gamma_{j'}\} = 2\delta_{jj'}$, is ensured. According to the above definition of γ_j 's, it is understood that the states of $|\Gamma_6, J_z = 1/2\rangle$, $|\Gamma_7, J_z = 3/2\rangle$, $|\Gamma_6, J_z = -1/2\rangle$, and $|\Gamma_7, J_z = -3/2\rangle$ are labeled as 1, 2, 3, and 4, respectively, for the matrix elements of $\mathcal{H}(\mathbf{k})$, namely, $\{\mathcal{H}_{mn}(\mathbf{k})\}$ with $m, n = 1 \sim 4$. Moreover, $d_j(\mathbf{k})$'s are given by

$$\begin{cases} d_3(\mathbf{k}) = t_{sp} \sin(k_x d_x) \\ d_4(\mathbf{k}) = \Delta_g + \sum_{l=x,y,z} \epsilon_l(k_l) \\ d_5(\mathbf{k}) = t_{sp} \sin(k_y d_y) \end{cases}, \quad (2)$$

where

$$\epsilon_l(k_l) = -2t^{xy}\{1 - \cos(k_l d_l)\} \quad (3)$$

for $l = x, y$, and

$$\epsilon_z(k_z) = -2t^z\{1 - \cos(k_z d_z)\}. \quad (4)$$

Here, t^l represents a hopping matrix between identical bands in the l -direction with $l = x, y, z$, where $t^l < 0$, $t^{xy} \equiv t^x = t^y$, and t_{sp} represents a hopping matrix between different bands due to a spin-orbit coupling. Further, d_l represents a lattice constant in the l -direction, and the bandgap at the Γ -point E_g is given by $E_g = E_{\Gamma_6} - E_{\Gamma_7}$ with $\Delta_g = E_g/2$, where the conduction and valence band energies at Γ_6 and Γ_7 are represented as E_{Γ_6} and E_{Γ_7} , respectively. An additional energy $c(\mathbf{k})$ is given by

$$c(\mathbf{k}) = E_F + 2 \sum_{l=x,y,z} m^l \{1 - \cos(k_l d_l)\} \quad (5)$$

with m^l 's constants, and the Fermi energy E_F is set equal to zero: $E_F = 0$. Hence, $E_{\Gamma_6} = c(\mathbf{0}) + d_4(\mathbf{0})$ and $E_{\Gamma_7} = c(\mathbf{0}) - d_4(\mathbf{0})$.

It is assumed that the off-diagonal block matrices of $\mathcal{H}(\mathbf{k})$ have little contributions to the band structure under the present tetragonal symmetry, that is, $d_1(\mathbf{k}), d_2(\mathbf{k}) \approx 0$, leading to $[I_2 \otimes \sigma_z, \mathcal{H}(\mathbf{k})] \approx 0$.¹⁰⁵ Thus, $\mathcal{H}(\mathbf{k})$ is cast into the block-diagonal form

$$\mathcal{H}(\mathbf{k}) = \begin{pmatrix} h(\mathbf{k}) & 0 \\ 0 & h^*(-\mathbf{k}) \end{pmatrix}, \quad (6)$$

where $h(\mathbf{k}) = d_3(\mathbf{k})\tau_x + d_4(\mathbf{k})\tau_z + d_5(\mathbf{k})\tau_y$.

An interaction of electron with light is introduced into $\mathcal{H}(\mathbf{k})$ by replacing \mathbf{k} by $\mathbf{K}(t) = \mathbf{k} + \mathbf{A}(t)$, followed by adding to $\mathcal{H}(\mathbf{K}(t))$ an interband electric dipole interaction represented by $\mathcal{H}'(t)$.¹⁰⁶ Here, the replacement by $\mathbf{K}(t)$ results from the Peierls phase transform in the lattice representation of the effective Hamiltonian, and the optical interaction arising from this replacement is herein termed as the Peierls interaction, as mentioned in Sec. I. Further, the interband electric-dipole interaction is provided as $\mathcal{H}'(t) = \mathbf{F}(t) \cdot \mathbf{M}$, where \mathbf{M} represents a matrix of electric-dipole transition between $|\Gamma_6, J_z = \pm 1/2\rangle$ and $|\Gamma_7, J_z = \pm 3/2\rangle$, independent of \mathbf{k} ; a double sign corresponds. The vector potential is given by

$$\mathbf{A}(t) = \left(-\frac{F_x}{\omega} \sin \omega t, \frac{F_y}{\omega} \cos \omega t, 0 \right) \quad (7)$$

with F_x and F_y constants, and in view of $\mathbf{F}(t) = -\dot{\mathbf{A}}(t)$, the associated electric field becomes

$$\mathbf{F}(t) = (F_x \cos \omega t, F_y \sin \omega t, 0). \quad (8)$$

The laser is linearly polarized in the x -direction when $F_x \neq 0$ and $F_y = 0$, while left-hand circularly polarized in the x - y plane when F_x is set equal to F_y , namely, $F_c \equiv F_x = F_y$. The time-dependent effective Hamiltonian of the driven semiconductor is thus read as¹⁰⁶

$$H(\mathbf{k}, t) = C(\mathbf{k}, t)I + \sum_{j=3}^5 D_j(\mathbf{k}, t)\gamma_j + \mathcal{H}'(t), \quad (9)$$

where $C(\mathbf{k}, t) \equiv c(\mathbf{K}(t))$ and $D_j(\mathbf{k}, t) \equiv d_j(\mathbf{K}(t))$.

Obviously, this Hamiltonian ensures the temporal periodicity, $H(\mathbf{k}, t + T) = H(\mathbf{k}, t)$ with $T = 2\pi/\omega$, and the system of concern follows the Floquet theorem.⁷² Thus, the present time-dependent problem ends up with the following Floquet eigenvalue problem as:

$$L(\mathbf{k}, t)\Psi_\alpha(t) = E_\alpha(\mathbf{k})\Psi_\alpha(t), \quad (10)$$

where

$$L(\mathbf{k}, t) = H(\mathbf{k}, t) - iI \frac{\partial}{\partial t}, \quad (11)$$

$E_\alpha(\mathbf{k})$ represents the α th eigenvalue termed a quasienergy or a Floquet energy, and $\Psi_\alpha(t)$ represents the associated eigenvector ensuring the temporal periodicity, $\Psi_\alpha(t + T) = \Psi_\alpha(t)$. In actual calculations, a set of $E_\alpha(\mathbf{k})$'s are obtained by numerically solving Eq. (10) in the ω -domain, where the Floquet matrix $L(\mathbf{k}, t)$ is recast into a Fourier-Floquet matrix element $\tilde{L}_{nn'}(\mathbf{k}, \omega)$ with respect to n and n' photon states.⁷² This is read as

$$\begin{aligned} \tilde{L}_{nn'}(\mathbf{k}, \omega) &= \tilde{C}_{nn'}(\mathbf{k}, \omega)I + \sum_{j=3}^5 \tilde{D}_{j,nn'}(\mathbf{k}, \omega)\gamma_j \\ &\quad + \tilde{\mathcal{H}}'_{nn'}(\omega) + n\omega I \delta_{nn'}, \end{aligned} \quad (12)$$

where it is understood that the Fourier transform of matrix $X(t)$ is represented by

$$\tilde{X}_{nn'}(\omega) = \frac{1}{T} \int_0^T dt e^{-i(n-n')\omega t} X(t). \quad (13)$$

In addition, it is remarked that in fact, $\tilde{C}_{nn'}(\mathbf{k}, \omega)$ is less dependent on the set of photon numbers, n and n' , and almost identical to $c(\mathbf{k})$. Hence, hereafter, it is understood that $E_\alpha(\mathbf{k})$'s are reckoned from $c(\mathbf{k})$; in other words, the effect of $c(\mathbf{k})$ on $E_\alpha(\mathbf{k})$'s is neglected. Explicit expressions of $\tilde{D}_{j,nn'}(\mathbf{k}, \omega)$ ($j = 3 \sim 5$) are given in Appendix A.

B. Electric dipole couplings

It is convenient to describe an explicit form of $\mathcal{H}'(t)$. This is provided as

$$\mathcal{H}'(t) = (\Omega_y \sin \omega t) \tau_x \otimes I_2 + (\Omega_x \cos \omega t) \tau_y \otimes \sigma_z, \quad (14)$$

where $\Omega_x = F_x P / \sqrt{2}$ and $\Omega_y = F_y P / \sqrt{2}$. Here, P is a dipole matrix element given by $P = \langle S|x|X \rangle = \langle S|y|Y \rangle$, where x and y represent the x and y components of electron position \mathbf{r} , respectively, and the states of $|\Gamma_6, J_z = \pm 1/2\rangle$ and $|\Gamma_7, J_z = \pm 3/2\rangle$ are represented by $|\Gamma_6, J_z = \pm 1/2\rangle = i|S\rangle$ and $|\Gamma_7, J_z = \pm 3/2\rangle = \pm(1/\sqrt{2})|X \pm iY\rangle$, respectively, in terms of s, p_x , and p_y states denoted as $|S\rangle, |X\rangle$, and $|Y\rangle$, respectively. Similar to Eq. (6), $\mathcal{H}'(t)$ is block-diagonalized as

$$\mathcal{H}'(t) = \begin{pmatrix} V^{(+)}(t) & 0 \\ 0 & V^{(-)}(t) \end{pmatrix}, \quad (15)$$

where $V^{(+)}(t)$ and $V^{(-)}(t)$ represent the electric dipole couplings between the up-spin bands, $|\Gamma_6, J_z = 1/2\rangle$ and $|\Gamma_7, J_z = 3/2\rangle$, and the down-spin bands, $|\Gamma_6, J_z = -1/2\rangle$ and $|\Gamma_7, J_z = -3/2\rangle$, respectively, given by

$$V^{(\pm)}(t) = (\Omega_y \sin \omega t) \tau_x \pm (\Omega_x \cos \omega t) \tau_y, \quad (16)$$

where a double sign corresponds. The Fourier transform of $V^{(\pm)}(t)$ into the ω -domain is given in Appendix A. In view of Eqs. (9) and (15), $H(\mathbf{k}, t)$ is cast into the block-diagonalized form:

$$H(\mathbf{k}, t) = C(\mathbf{k}, t)I + \begin{pmatrix} H^{(+)}(\mathbf{k}, t) & 0 \\ 0 & H^{(-)}(\mathbf{k}, t) \end{pmatrix}, \quad (17)$$

that is, $[I_2 \otimes \sigma_z, H(\mathbf{k}, t)] = 0$. Here, the up-spin Hamiltonian $H^{(+)}(\mathbf{k}, t)$ and the down-spin Hamiltonian $H^{(-)}(\mathbf{k}, t)$ are given by

$$H^{(\pm)}(\mathbf{k}, t) = [\pm D_3(\mathbf{k}, t) + \Omega_y \sin \omega t] \tau_x + D_4(\mathbf{k}, t) \tau_z + [D_5(\mathbf{k}, t) \pm \Omega_x \cos \omega t] \tau_y. \quad (18)$$

The expression of Eq. (16) implies that in general, an optical dipole interaction between up-spin bands is different from that between down-spin bands. To be specific,

for a linearly polarized light,

$$V^{(\pm)}(t) = \pm(\Omega_x \cos \omega t) \tau_y = \pm \Omega_x \cos \omega t \begin{pmatrix} 0 & -i \\ i & 0 \end{pmatrix} \quad (19)$$

with $\Omega_y = 0$, and $V^{(+)}(t)$ is identical to $V^{(-)}(t)$ aside from an unimportant phase factor $\mp i$. On the other hand, for a left-hand circularly polarized light,

$$V^{(\pm)}(t) = \Omega_c [(\sin \omega t) \tau_x \pm (\cos \omega t) \tau_y] = \mp i \Omega_c \begin{pmatrix} 0 & e^{\pm i \omega t} \\ -e^{\mp i \omega t} & 0 \end{pmatrix} \quad (20)$$

with $\Omega_c \equiv \Omega_x = \Omega_y$, and $V^{(+)}(t)$ and $V^{(-)}(t)$ are different from each other. In particular, this distinction stands out for a linear optical transition, for instance, from the valence band at Γ_7 to the conduction band at Γ_6 . In view of the matrix element $V_{12}^{(\pm)}(t)$ of Eq. (20), the transition amplitudes of the photoabsorption between the up-spin bands, represented as $a^{(+)}$, and that between the down-spin bands, represented as $a^{(-)}$, are given by

$$a^{(\pm)} = \mp i \Omega_c \int_{-\infty}^{\infty} dt e^{i(E_{\Gamma_6} - E_{\Gamma_7} \pm \omega)t} \propto \delta(E_g \pm \omega) \quad (21)$$

with $E_g = E_{\Gamma_6} - E_{\Gamma_7} > 0$. It is evident that the transition between the up-spin bands is forbidden, namely, $a^{(+)} = 0$, while that between the down-spin bands is allowed, namely, $a^{(-)} \neq 0$, because of the energy conservation $\omega = E_g$. Incidentally, as regards the related photoemission, in view of the matrix element $V_{21}^{(\pm)}(t)$, the transition amplitudes of it are given by

$$b^{(\pm)} = \pm i \Omega_c \int_{-\infty}^{\infty} dt e^{i(E_{\Gamma_7} - E_{\Gamma_6} \mp \omega)t} \propto \delta(E_g \pm \omega), \quad (22)$$

and the same discussion as the photoabsorption is applicable; $b^{(+)} = 0$ and $b^{(-)} \neq 0$.

As long as $\omega \approx E_g$, these results almost hold correct in non-linear optical processes including strongly photoinduced processes, though the contribution from up-spin bands does not vanish because the energy conservation is not required in virtual states. In other words, the effect of $V^{(-)}(t)$ is dominant over that of $V^{(+)}(t)$. This is one of the key issues in this paper, as mentioned in Sec. I. In contrast, as regards off-resonant cases that $\omega \gg E_g$ or $\omega \ll E_g$, $V^{(+)}(t)$ and $V^{(-)}(t)$ would have almost equal, however, vanishingly small contributions to optical processes, as long as $|E_g - \omega| \gg 2\Omega_c$; for more detail, see Eq. (23) or (24) to be shown later.

C. Symmetries

It is evident that both T- and I-symmetries are conserved in $\mathcal{H}(\mathbf{k})$, that is, $\Theta^{-1} \mathcal{H}(-\mathbf{k}) \Theta = \mathcal{H}(\mathbf{k})$, and $\Pi^{-1} \mathcal{H}(-\mathbf{k}) \Pi = \mathcal{H}(\mathbf{k})$, where Θ and Π represent the T- and I-operators, defined by $\Theta = -iI_2 \otimes \sigma_y K$ and $\Pi =$

$\tau_z \otimes I_2$, respectively, where K means an operation of taking complex conjugate. Further, the T-symmetry is still respected in $H(\mathbf{k}, t)$ for a linearly polarized light, that is, $\Theta^{-1}H(-\mathbf{k}, -t)\Theta = H(\mathbf{k}, t)$, and thus, a pair of up-spin and down-spin Floquet bands forms Kramers degeneracy. On the other hand, the T-symmetry is broken for a circularly polarized light, that is, $\Theta^{-1}H(-\mathbf{k}, -t)\Theta \neq H(\mathbf{k}, t)$.

As regards the I-symmetry, this is broken, that is, $\Pi^{-1}H(-\mathbf{k}, t)\Pi \neq H(\mathbf{k}, t)$, because $D_j(-\mathbf{k}, t) \neq -D_j(\mathbf{k}, t)$ for $j = 3$ and 5 , $D_4(-\mathbf{k}, t) \neq D_4(\mathbf{k}, t)$, and $\Pi^{-1}\mathcal{H}'(t)\Pi \neq \mathcal{H}'(t)$. In fact, it is shown that in terms of an operator defined as $\tilde{\Pi} = \Pi\mathcal{T}_{1/2}$, the symmetry $\tilde{\Pi}^{-1}H(-\mathbf{k}, t + T/2)\tilde{\Pi} = H(\mathbf{k}, t)$ is retrieved, where $\mathcal{T}_{1/2}$ represents the operation of putting t ahead by a half period $T/2$, namely, the replacement of $t \rightarrow t + T/2$.^{65,73} This is the time-glide I -operator mentioned in Sec. I. Therefore, despite the breaking of the I-symmetry, a Floquet band disperses in a symmetric manner with respect to \mathbf{k} , namely, $E_\alpha(\mathbf{k}) = E_\alpha(-\mathbf{k})$. For a linearly polarized light, it is still probable that a four-fold band crossing occurs at the high-symmetry points, namely, the time-reversal invariant momenta.

III. RESULTS AND DISCUSSION

In the actual calculations, the following material parameters^{7,8} and laser parameters are employed as: $E_g = 0.0169$ (0.46 eV), $\omega = 0.0147$ (0.4 eV), $d_x = d_y = 5.67$ (3 Å), $d_z = 9.44$ (5 Å), $t^{xy} = -0.0018$, $t^z = -0.0074$, $t_{sp} = 0.0037$, $F_x = F_c = 0.0003$ (1.54 MV/cm), and $P = 25.9$. Further, the maximum number of photons (N_p) incorporated in the calculations is set to be three to reach numerical convergence, that is, $n, n' = -N_p \sim N_p$ for the Fourier-Floquet matrix $\tilde{L}_{nn'}(\mathbf{k}, \omega)$.

Based on these numerical parameters, one evaluates the degree of magnitude of effects due to the Peierls interaction. These contributions are determined in terms of factors given by the n th-order Bessel function of the first kind $J_n(z_l)$ that is included in $\tilde{D}_{j,nn'}(\mathbf{k}, \omega)$ ($j = 3 \sim 5$) of Eqs. (A3)-(A5) with $z_l \equiv F_l d_l / \omega$ ($l = x, y$). For $z_l = 0.116$, one obtains that $J_0(z_l) - 1 = -0.0034$, $J_1(z_l) = 0.056$, and $J_2(z_l) = 0.0017$, implying that the hopping matrices of t^l and t_{sp} are modified just by the order of $10^{-2} \sim 10^{-3}$ by the Peierls interaction. Thus, it is stated that in the system of concern, this interaction plays a less significant role than the interband electric-dipole interaction.

A. Qualitative Understanding of Band Structures

It is preferable to show an overall Floquet band structure in the present system in a qualitative manner prior to the discussion of rather complicated numerical results. Here, a Floquet state α attributed to a b -band dressed with n photons is denoted as $b(n)$ with $b = e, hh$, where

the bands e and hh represent the s and heavy-hole p orbitals, respectively. Below, one seeks approximate Floquet bands represented in an analytic closed form in a two-step manner. First, based on a two-band model incorporating $e(n-1)$ and $hh(n)$ for each spin state, one seeks expressions of hybridized bands of states $e(n-1)$ for up- and down-spins, represented as $\mathcal{E}_{e(n-1)}^{(+)}$ and $\mathcal{E}_{e(n-1)}^{(-)}$, respectively. Here, the ac-Stark effect with a Rabi frequency Ω_l is incorporated by employing the rotational-wave approximation. Similarly, the coupling between $e(n)$ and $hh(n+1)$ for each spin state results in expressions of hybridized bands of states $hh(n+1)$ for up- and down-spins, represented as $\mathcal{E}_{hh(n+1)}^{(+)}$ and $\mathcal{E}_{hh(n+1)}^{(-)}$, respectively. Second, by introducing the residual spin-orbit interaction between $\mathcal{E}_{e(n-1)}^{(\pm)}$ and $\mathcal{E}_{hh(n+1)}^{(\pm)}$ bands, one obtains the desired expressions of hybridized Floquet bands represented by $E_{e(n-1)}^{(\pm)}(\mathbf{k})$ and $E_{hh(n+1)}^{(\pm)}(\mathbf{k})$: a double sign corresponds. For more detail of the derivation, consult Appendices B 1-B 3.

In the case that the band $hh(n+1)$ is located above the band $e(n-1)$, the resulting energy, represented by $E^{(\pm)}(\mathbf{k})$, is cast into $E^{(\pm)}(\mathbf{k}) = E_{hh(n+1)}^{(\pm)}(\mathbf{k}) \geq n\omega$ and $E^{(\pm)}(\mathbf{k}) = E_{e(n-1)}^{(\pm)}(\mathbf{k}) \leq n\omega$, the expressions of which are given by Eqs. (B34) and (B35), respectively. To avoid unnecessary complication in these expressions, the approximations that $J_0(z_l) \approx 1$ and $J_{n(\neq 0)}(z_l) \approx 0$ are made. Thus, these are read as

$$E_{e(n-1)}^{(\pm)}(\mathbf{k}) \approx - \left[\left\{ \omega/2 - \left(\eta(\mathbf{k})^2 + |\mathcal{W}_0^{(\pm)}|^2 \right)^{1/2} \right\}^2 + |\mathcal{V}_0^{(\pm)}|^2 \right]^{1/2} + n\omega, \quad (23)$$

and

$$E_{hh(n+1)}^{(\pm)}(\mathbf{k}) \approx \left[\left\{ \omega/2 - \left(\eta(\mathbf{k})^2 + |\mathcal{W}_0^{(\pm)}|^2 \right)^{1/2} \right\}^2 + |\mathcal{V}_0^{(\pm)}|^2 \right]^{1/2} + n\omega, \quad (24)$$

where

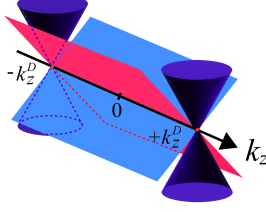
$$\eta(\mathbf{k}) = d_4(\mathbf{k}) - \frac{\omega}{2}, \quad (25)$$

and $d_4(\mathbf{k})$ is given in Eq. (2). Further, $\mathcal{W}_0^{(+)} = [\mathcal{W}_0^{(-)}]^* = -i\Omega_x/2$ for the linearly polarized light, while $\mathcal{W}_0^{(+)} = 0$ and $\mathcal{W}_0^{(-)} = i\Omega_c$ for the circularly polarized light. Defining $\mathcal{V}_0^{(\pm)}$ as an approximation expression of $\mathcal{V}^{(\pm)}$ of Eq. (B31) in view of the above approximations, one has

$$|\mathcal{V}_0^{(\pm)}| = t_{sp}\sigma^{(\pm)}\sqrt{\sin^2(k_x d_x) + \sin^2(k_y d_y)}, \quad (26)$$

where the prefactor $\sigma^{(\pm)}$ depending on the polarization of light is given by Eq. (B51). In Eqs. (23) and (24), $\mathcal{V}_0^{(\pm)}$ is attributed to $\mathcal{D}_3(\mathbf{k}, t)$ and $\mathcal{D}_5(\mathbf{k}, t)$ in Eq. (9), while

(a) FDSM (linear polarization)



(b) FWSM (left-handed circular polarization)

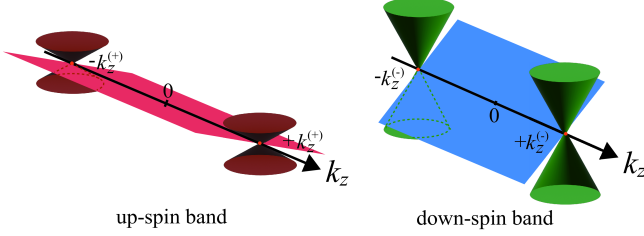


FIG. 1. The scheme of the surface state formation. (a) In the FDSM arising from the drive of linearly polarized laser, this phase hosts non-trivial surface states with up-spin (red) and down-spin (blue) that are pinned to a pair of surface Dirac nodes at $k_z = \pm k_z^{D(\pm)}$. (Here, $k_z^{D(\pm)}$ is replaced by the notation of $k_z^{D(\pm)}$ just for the sake of simplicity.) (b) In the FWSM arising from the drive of left-hand circularly polarized laser, due to the breaking of the T-symmetry, the Dirac nodes of the above FDSM are split into a pair of Weyl nodes, and each FWSM phase hosts a non-trivial surface state. One surface state (red) is characteristic of an up-spin band and is pinned to a pair of surface Dirac nodes at $k_z = \pm k_z^{D(+)}$. The other state (blue) is characteristic of a down-spin band and is pinned to a pair of surface Dirac nodes at $k_z = \pm k_z^{D(-)}$. (Here, $k_z^{W(\pm)}$ is replaced by the notation of $k_z^{D(\pm)}$ just for the sake of simplicity.) For more detail, consult the text.

$\mathcal{W}_0^{(\pm)}$ is attributed to $\mathcal{H}'(t)$. Hereafter, it is understood that in the opposite case that $hh(n+1)$ is located below $e(h-1)$, the subscript of $e(n-1)$ is replaced by that of $hh(n+1)$ in the above equations, that is, $E^{(\pm)}(\mathbf{k}) = E_{hh(n+1)}^{(\pm)}(\mathbf{k}) \leq n\omega$ and $E^{(\pm)}(\mathbf{k}) = E_{e(n-1)}^{(\pm)}(\mathbf{k}) \geq n\omega$.

Now, one examines the possibility of creating Dirac nodal points on the k_z -axis that result from band inversion for the irradiation of the linearly polarized light. It is likely that the band $e(n-1)$ crosses the band $hh(n'+1)$ for $n = n'$ at $\mathbf{k} = (0, 0, k_z)$ when $E_{e(n-1)}(\mathbf{k}) = E_{hh(n+1)}(\mathbf{k})$. Here, one takes account of the pair of Floquet bands of $e(-1)$ and $hh(1)$. These bands are enabled to be inverted to form a pair of Dirac nodes at the positions $\pm \mathbf{k}^{D(\pm)} \equiv \pm(0, 0, k_z^{D(\pm)})$ subject to the equation

$$\epsilon_z(k_z^{D(\pm)}) = \frac{1}{2} \left[\omega - E_g + \sqrt{\omega^2 - \Omega_x^2} \right] \quad (27)$$

in terms of $\epsilon_z(k_z)$ defined in Eq. (4) under the condition that

$$\omega_1^D < \omega < \omega_2^D, \quad (28)$$

where

$$\omega_1^D = \text{Max} \left(\Omega_x, \frac{\Delta_g^2 + (\Omega_x/2)^2}{\Delta_g} \right), \quad (29)$$

and

$$\omega_2^D = \frac{(\Delta_g - 4t^z)^2 + (\Omega_x/2)^2}{\Delta_g - 4t^z}. \quad (30)$$

For more accurate expressions than Eqs. (27) and (28), consult Eqs. (B36) and (B41), respectively.

The existence of these nodes exhibits the manifestation of the Floquet DSM (FDSM) phases in the original crystal of Zn_3As_2 that is in a topologically trivial phase. Due to the T-symmetry in addition with the time-glide I-symmetry, the up-spin and down-spin bands for the states $e(-1)$ and $hh(1)$ are doubly degenerate, that is, $E_{e(-1)}^{(+)}(\mathbf{k}) = E_{e(-1)}^{(-)}(\mathbf{k})$ and $E_{hh(1)}^{(+)}(\mathbf{k}) = E_{hh(1)}^{(-)}(\mathbf{k})$, and the above Dirac nodes are four-fold degenerate, namely, $k_z^{D(+)} = k_z^{D(-)}$. Thus, it is considered that the FDSM carries Chern number zero and is not topologically protected.¹⁸ In addition, as shown in Eq. (B53), $E^{(\pm)}(\mathbf{k}) \geq 0$ forms an upper part of the Dirac cone (linear dispersion) in the vicinity of $\mathbf{k} = \mathbf{k}^{D(\pm)}$, that is,

$$E^{(\pm)}(\mathbf{k}) \approx \left[\sum_{l=x,y} (\xi_l^D)^2 (k_l d_l)^2 + (\xi_z^D)^2 (\Delta k_z d_z)^2 \right]^{1/2}, \quad (31)$$

where $\Delta k_z = k_z - k_z^{D(\pm)}$, and the constants of $\xi_x^D = \xi_y^D$ and ξ_z^D are given right below Eq. (B53).

Further, in the similar manner to DSMs created by the band inversion mechanism in stationary systems such as Cd_3As_2 and Na_3Bi ,^{7,8,11,14,18} two-dimensional (2D) nontrivial surface states are also expected in the FDSM phase. As shown schematically in Fig. 1(a), these surface states are composed of up-spin and down-spin states forming a Kramers pair, each energy band of which is attached to the same pair of the Dirac nodes that are projected to the surface 2D-BZ; hereafter, these projected Dirac nodes are termed as surface Dirac nodes or surface Dirac points. The intersection of the Fermi energy with these two leaves of surface bands would result in the formation of double Fermi arcs, supposing that the whole of carriers are occupied just below E_F in disregard of the non-equilibrium system of concern.

Next, as regards the circularly polarized laser drive, the T-symmetry is broken to lift the two-fold degeneracy between up-spin and down-spin bands. Thus, the four-fold degeneracy at the Dirac nodes (at $\pm \mathbf{k}^{D(\pm)}$) are also lifted to be split into two pairs of Weyl nodes residing at $\pm \mathbf{k}^{W(-)} \equiv \pm(0, 0, k_z^{W(-)})$ and $\pm \mathbf{k}^{W(+)} \equiv \pm(0, 0, k_z^{W(+)});$ a double sign corresponds. The nodal momentum $\pm \mathbf{k}^{W(-)}$ is attributed to the down-spin Floquet band, and its location is subject to the similar equation

as Eq. (27), aside from the replacement of Ω_x by $2\Omega_c$,

$$\epsilon_z(k_z^{W(-)}) = \frac{1}{2} \left[\omega - E_g + \sqrt{\omega^2 - 4\Omega_c^2} \right] \quad (32)$$

under the condition that

$$\omega_1^{W(-)} < \omega < \omega_2^{W(-)}, \quad (33)$$

where

$$\omega_1^{W(-)} = \text{Max} \left(2\Omega_c, \frac{\Delta_g^2 + \Omega_c^2}{\Delta_g} \right), \quad (34)$$

and

$$\omega_2^{W(-)} = \frac{(\Delta_g - 4t^z)^2 + \Omega_c^2}{\Delta_g - 4t^z}. \quad (35)$$

Here the ac-Stark effect plays a key role. On the other hand, the nodal momentum $\pm \mathbf{k}^{W(+)}$ is attributed to the up-spin Floquet band, and its location is subject to the equation

$$\epsilon_z(k_z^{W(+)}) = \omega - \Delta_g \quad (36)$$

under the condition that

$$\omega_1^{W(+)} < \omega < \omega_2^{W(+)}, \quad (37)$$

where $\omega_1^{W(+)} = \Delta_g$ and $\omega_2^{W(+)} = \Delta_g - 4t^z$. Here, in contrast, the ac-Stark effect is less significant because the optical interaction given by $V^{(+)}(t)$ of Eq. (20) has negligibly small contributions in the case of $\omega \approx E_g$; consult Sec. II B. Thus, it is obvious that $k_z^{W(+)} > k_z^{D(\pm)} > k_z^{W(-)}$; based on Eqs. (27), (32) and (36), approximate values of $k_z^{W(+)}$, $k_z^{D(\pm)}$, and $k_z^{W(-)}$ are estimated as $k_z^{W(+)} = 0.956/d_z$, $k_z^{D(\pm)} = 0.910/d_z$, and $k_z^{W(-)} = 0.732/d_z$, respectively.

In addition, as shown in Eq. (B56), $E^{(-)}(\mathbf{k})$ forms an upper part of the Weyl cone (linear dispersion) in the vicinity of $\mathbf{k} = \mathbf{k}^{W(-)}$, that is,

$$E^{(-)}(\mathbf{k}) \approx \left[\sum_{l=x,y} (\xi_l^W)^2 (k_l d_l)^2 + (\xi_z^W)^2 (\Delta k_z d_z)^2 \right]^{1/2}, \quad (38)$$

where $\Delta k_z = k_z - k_z^{W(-)}$, and the constants of $\xi_x^W = \xi_y^W$ and ξ_z^W are given right below Eq. (B56). On the other hand, as shown in Eq. (B55), in contrast with $E^{(-)}(\mathbf{k})$, $E^{(+)}(\mathbf{k})$ forms a quadratic dispersion with respect to k_x and k_y and a linear dispersion with respect to Δk_z in the vicinity of $\mathbf{k} = \mathbf{k}^{W(+)}$, that is,

$$E^{(+)}(\mathbf{k}) \approx \left| (-t^{xy}) \sum_{l=x,y} (k_l d_l)^2 + \eta_z^{(1)} (\Delta k_z d_z) \right|, \quad (39)$$

where $\Delta k_z = k_z - k_z^{W(+)}$, and $\eta_z^{(1)} = -2t^z \sin(k_z^{W(+)} d_z)$. Here, a term of linear dispersion represented by $\sum_{l=x,y} \nu_l^{(+)}(k_l d_l)$ is considered negligibly small, because the expansion coefficient is given by $|\nu_l^{(+)}| = t_{sp} [t_{sp} J_1(z_c) / (2\eta(\mathbf{k}^{W(+)}))]^2$ due to the reduction of the spin-orbit interaction by the Peierls interaction by a factor of the order of $J_1(z_c)$; see also the explanation below Eq. (B55).

Further, the FWSM band structure $E^{(+)}(\mathbf{k})$ in the vicinity of the $k_x - k_y$ plane ($k_z = 0$) is examined. Following Eq. (24) for $d_4(\mathbf{k}) > \omega/2$, this is represented simply as

$$E^{(+)}(\mathbf{k}) \approx \omega - d_4(\mathbf{k}) \quad (40)$$

within the order of $t_{sp} J_1(z_c) \approx 0$ due again to the reduction of t_{sp} by the Peierls interaction. Thus, there is a closed ring in the $k_x - k_y$ plane ($k_z = 0$) on which $E^{(+)}(\mathbf{k}) \approx 0$; the locus of this ring is given by

$$-2t^{xy} \sum_{l=x,y} [1 - \cos(k_l d_l)] = \omega - \Delta_g > 0. \quad (41)$$

As regards the FWSM of the down-spin state, an effect of Ω_c causes a gap to open between $E_{hh(1)}^{(-)}(\mathbf{k})$ and $E_{e(-1)}^{(-)}(\mathbf{k})$ in this plane. Consult Eq. (B59) and the related discussion in Appendix B 3 on the closed ring formation in the $k_x - k_y$ plane ($k_z \neq 0$) and the origin of the difference between the up- and down-spin states.

Given the relation between Dirac points and Weyl points in stationary systems, the surface Dirac point in the FDSM is regarded as the stable merger of two Weyl points in the FWSM that have different handedness and are projected to the same surface momentum. Hereafter, these Weyl points are termed as surface Weyl nodes or surface Weyl points. Due to the breaking of the T-symmetry and the resulting splitting of the Dirac node into of the pair of Weyl nodes, the associated energy bands of the two surfaces with different spin states are pinned to different surface Weyl points, as shown schematically in Fig. 1(b). That is, the surface band characteristic of up-spin/down-spin state is pinned to the surface Weyl point projected from the bulk Weyl points at $\pm \mathbf{k}^{W(+)}/\pm \mathbf{k}^{W(-)}$. Further, it is considered that the energy gap $\mathcal{E}_g^{(+)}$ arising from the hybridization between the up-spin Floquet bands $e(-1)$ and $hh(1)$ are largely different from the energy gap $\mathcal{E}_g^{(-)}$ attributed to the down-spin bands mostly due to the difference of magnitude between $V^{(+)}(t)$ and $V^{(-)}(t)$; to be more specific, $\mathcal{E}_g^{(+)} \ll \mathcal{E}_g^{(-)}$. Such difference is straightforward reflected on the band gaps projected to the surface BZ; see Fig. 1(b). Therefore, it is speculated that the most parts of down-spin surface band are energetically separated from the up-spin surface band; for more detail, consult Sec. III C.

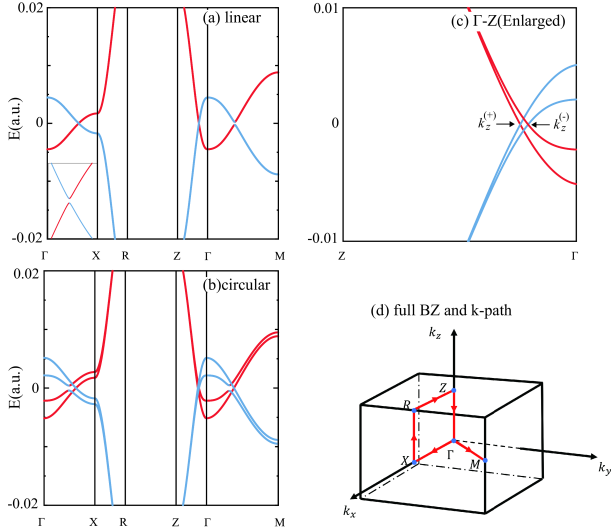


FIG. 2. Band structures of FDSM and FWSM. (a) The calculated band structure of FDSM with the drive of a linearly polarized laser. Inset: Expanded view of the band structure in the vicinity of the anticrossing along the Γ -X line. (b) The calculated band structure of FWSM with the drive of a left-hand circularly polarized laser. (c) Expanded view of panel (b) in the vicinity of the band crossing along the Γ -Z line with specification of the Weyl nodes at $k_z^{(+)}$ and $k_z^{(-)}$; these are the abbreviation of $k_z^{W(+)}$ and $k_z^{W(-)}$, respectively. In panels (a), (b), and (c), bands dominated rather by the s/p -orbital component are denoted by a red/blue solid line. (d) The bulk BZ of the crystal Zn_3As_2 .

B. Floquet Band Structures of FDSM and FWSM

Figures 2(a) and 2(b) show the calculated Floquet band structures of FDSM and FWSM, respectively, for the crystal structure of Zn_3As_2 given in Fig. 2(d). In Fig. 2(a), it is found that there is a Dirac node along the Γ -Z line at $k_z^{D(\pm)}$ in addition with anticrossings along the lines of Γ -X and Γ -M with energy differences of approximately 3 and 30 meV, respectively. As shown in Fig. 2(b), the two-fold degeneracy confirmed in panel (a) is lifted to result in energy splitting between the up-spin and down-spin bands. It is noted that a pair of Weyl nodes emerges along the Γ -Z line at different k_z 's following $k_z^{W(-)} < k_z^{W(+)}$, as shown in the enlarged view of Fig. 2(c). As regards the up-spin bands, the anticrossing along the line of Γ -M is largely reduced from that in panel (a) to approximately 0.4 meV, while the energy difference along the line of Γ -X is almost the same as 2 meV. In contrast, as regards the down-spin bands, the energy differences of anticrossings along the lines of Γ -X is largely enhanced from that in panel (a) to approximately 23 meV, while that along the line of Γ -M is slightly changed to approximately 20 meV.

Figures 3(a) and 3(b) show the energy dispersions of the up-spin and down-spin bands at $k_z = 0$. In Fig. 3(a),

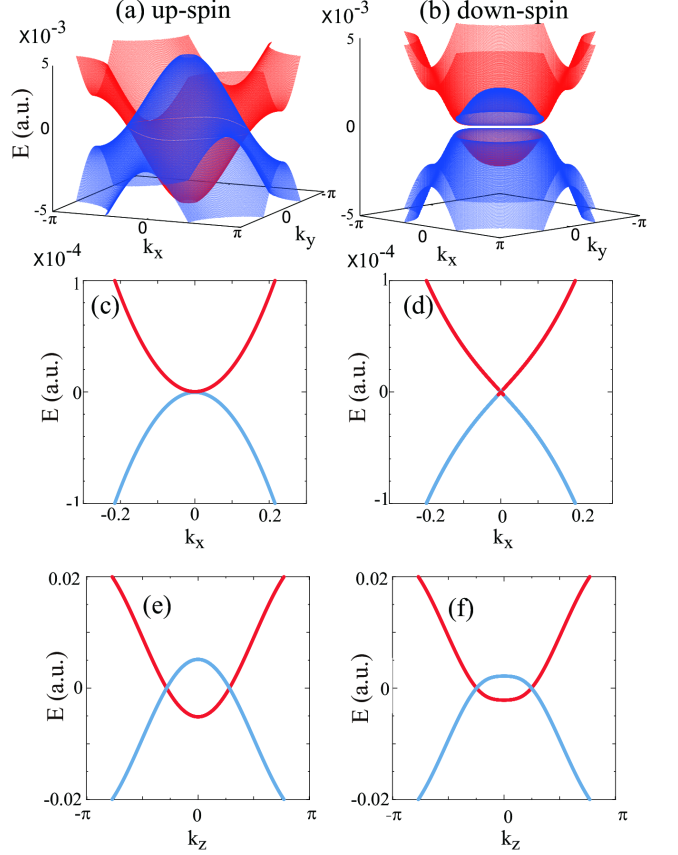


FIG. 3. Energy dispersions $E^{(\pm)}(\mathbf{k})$ of up-spin and down-spin bands at $k_z = 0$ and in the vicinity of the Weyl points. The axis of abscissa k_l is gauged in the unit of $1/d_l$ with $l = x, y, z$. Here, $E^{(\pm)}(\mathbf{k})$ is simply represented as $E(\mathbf{k})$, and bands dominated rather by the s/p -orbital component are denoted by a red/blue solid line. (a) $E(\mathbf{k})$ in the $k_x - k_y$ plane at $k_z = 0$ for the up-spin bands. (b) The same as panel (a) but for the down-spin bands. (c) $E(\mathbf{k})$ as a function of k_x with $k_y = 0$ in the vicinity of the Weyl point $\mathbf{k}^{W(+)}$ for the up-spin bands. (d) The same as panel (c) but in the vicinity of the Weyl point $\mathbf{k}^{W(-)}$ for the down-spin bands. (e) $E(\mathbf{k})$ as a function of k_z with $k_x = k_y = 0$ for the up-spin bands with the Weyl points $\pm k_z^{W(+)} = \pm 0.887/d_z$. (f) The same as panel (e) but for the down-spin bands with the Weyl points $\pm k_z^{W(-)} = \pm 0.775/d_z$.

the up-spin band structure is reminiscent of a NLSM phase with a nodal ring on the $k_x - k_y$ plane; see also the enlarged figure of it given in Appendix C. According to the analytic model developed in Sec. III A, the locus of the ring is approximately represented as Eq. (41). In fact, this ring is slightly blurred at most by $\mathcal{E}_g^{(+)} \approx 2$ meV around $E = 0$ that corresponds to the above-mentioned energy difference along the line of Γ -X. On the other hand, it is obviously seen in Fig. 3(b) that the down-spin band is gapped by the order of $\mathcal{E}_g^{(-)} \approx 20$ meV due to the

relatively strong anticrossing between $e(-1)$ and $hh(1)$; see also the enlarged figure of it given in Appendix C.

The definite contrast in the energy dispersions between up-spin and down-spin bands seen in Figs. 3(a) and 3(b) is caused by the different manner of couplings between the Floquet states of $e(-1)$ and $hh(1)$. It is noted that the leading contribution arises from a two-photon coupling between $e(-1)$ and $hh(1)$, because the difference of the photon number of these Floquet bands equals two. This coupling is given by a successive interaction composed of the coupling due to $\tilde{D}_{4,nn'}(\mathbf{k}, \omega)$ and one of the three terms, $\tilde{D}_{j,nn'}(\mathbf{k}, \omega)$, ($j = 3, 5$) and $\tilde{\mathcal{H}}'_{nn'}(\omega)$, in Eq. (12) with $|n - n'| = 1$. For example, for down-spin bands, it is likely that $hh(1)$ is mediated by a two-photon interaction, $\tilde{\mathcal{H}}'_{01}(\omega)$ followed by $\tilde{D}_{4,-10}(\mathbf{k}, \omega)$, to be coupled with $e(-1)$. As regards up-spin bands, because the effect of $\tilde{\mathcal{H}}'_{01}(\omega)$ is negligibly small, $hh(1)$ is coupled with $e(-1)$ by a two-photon interaction, $\tilde{D}_{j,01}(\mathbf{k}, \omega)$, ($j = 3, 5$) followed by $\tilde{D}_{4,-10}(\mathbf{k}, \omega)$. The magnitudes of interactions $\tilde{\mathcal{H}}'_{01}(\omega)$ and $\tilde{D}_{j,01}(\mathbf{k}, \omega)$, ($j = 3, 5$) are roughly evaluated to be Ω_c and $J_1(z_c)t_{sp}$, respectively; consult Eqs. (20), (A3), and (A5). Thus, it is stated that the inverted band gap $\mathcal{E}_g^{(-)}$ in the down-spin state is mostly caused by a strong resonant electric dipole coupling, while $\mathcal{E}_g^{(+)}$ in the up-spin state is just attributed to an optical spin-orbit coupling, namely, a spin-orbit coupling reduced by a factor of $J_1(z_c)$; actually, $\Omega_c = 5.49 \times 10^{-3} \gg t_{sp}J_1(z_c) = 2.07 \times 10^{-4}$. The resulting FWSM phase for the up-spin state is considered as a Floquet NLSM (FNLSM) phase that is generated by the drive of the present circularly polarized light.

Such sharp distinction between the up-spin and down-spin bands is also seen in the energy dispersions in the k_x -direction in the vicinity of the Weyl points at $\mathbf{k}^{W(+)}$ and $\mathbf{k}^{W(-)}$, respectively, as shown in Figs. 3(c) and 3(d). It is noted that the up-spin band crosses with quadratic band touching, following

$$E^{(+)}(\mathbf{k}) \approx (-t^{xy})(k_x d_x)^2 \geq 0, \quad (42)$$

as given in Eq. (39), while the down-spin band crosses with linear band touching, as often happens, following

$$E^{(-)}(\mathbf{k}) \approx \xi_x^W |k_x d_x| \geq 0, \quad (43)$$

as given in Eq. (38), where ξ_x^W is of the order of t_{sp} . In fact, there is a contribution from the linear dispersion of the form of $\nu_x^{(+)}(k_x d_x)$ in Eq. (42), however, this is neglected because of $\nu_x^{(+)} \ll 1$, as mentioned before.

Further, it is seen in Figs. 3(e) and 3(f) that the two bands of $e(-1)$ and $hh(1)$ are inverted to form a pair of Weyl nodes along the k_z -axis at $k_z^{W(\pm)}$ and $-k_z^{W(\pm)}$. These dispersions in the vicinity of $\mathbf{k}^{W(\pm)}$ are given by

$$E^{(+)}(\mathbf{k}) \approx \eta_z^{(1)} |\Delta k_z d_z| \geq 0 \quad (44)$$

for the up-spin state, and

$$E^{(-)}(\mathbf{k}) \approx \xi_z^W |\Delta k_z d_z| \geq 0 \quad (45)$$

for the down-spin state, following Eqs. (39) and (38), respectively. Here, the obtained numerical value of $k_z^{W(+)}$ ($= 0.887/d_z$) is greater than that of $k_z^{W(-)}$ ($= 0.775/d_z$), which is in harmony with the qualitative discussion based on the approximated expressions of Eqs. (32) and (36); consult the values thus obtained for $k_z^{W(\pm)}$ below Eq. (37). It is speculated that the difference of the former numerical values from the latter approximate ones is attributed to the non-resonant contributions of interband couplings beyond the rotational-wave approximation in the nearly resonant two-band model adopted in Sec. III A. Actually, the intense laser field is applied to the system of concern with the order of $\Omega_c/\omega \approx 0.37$, and hence, for instance, the Floquet band $hh(1)$ is somewhat coupled with other non-resonant bands of $e(n \neq 0)$ in addition with the nearly resonant band $e(0)$.

C. Surface States

Here, it is considered that a vanishing boundary condition in the y -direction is imposed on the Floquet eigenvalue problem given by Eq. (10) in place of a periodic boundary condition. To be specific, an electron is confined in the finite range of y from $L_1 = 0$ to $L_2 = 40$ a.u., while it moves freely in the $x - z$ plane. Such confinement results in energy dispersions $\mathcal{E}(\bar{\mathbf{k}})$ that are the projection of bulk bands $E(\mathbf{k})$ on the $k_x - k_z$ plane where $\bar{\mathbf{k}} = (k_x, k_z)$. Further, it is likely that surface states are hosted by the projected bands. For the sake of the later convenience, the positions of surface Weyl nodes for the up-spin and down-spin bands are represented as $\pm \bar{\mathbf{k}}^{W(+)} = \pm(0, k_z^{W(+)})$ and $\pm \bar{\mathbf{k}}^{W(-)} = \pm(0, k_z^{W(-)})$, respectively.

Figure 4 shows the projected energy dispersions of down-spin bands with surface states at three different k_z 's. As shown in Fig. 4(a), at k_z close to $k_z^{W(-)}$, the inverted bands of $e(-1)$ and $hh(1)$ form a definite energy gap $\mathcal{E}_g^{(-)}$, hosting a pair of surface states just in a small range of k_x . It is evident that as k_z becomes closer to $k_z^{(-)}$, the range of k_x becomes more reduced, and eventually, the pair of surface states are embedded in the surface Weyl point at $\bar{\mathbf{k}}^{W(-)}$. Meanwhile, it is remarked that the appearance of such a pair is due to a numerical artifact ascribable to the above-mentioned confinement of electron in the finite range in place of a semi-infinite confinement corresponding to $L_2 = \infty$. Here, it is understood that in all of the figures in Fig. 4, just the surface states with a positive gradient are taken account of. As shown in Figs. 4(b)-4(d), with the further decrease of k_z , the range of k_x in which the surface state is supported becomes larger, and is maximized at $k_z = 0$, where this range extends over a half of the BZ in the k_x direction. Moreover, as k_z changes from $k_z = 0$ to the negative k_z -direction, the range of k_x turns to a decrease, and eventually, at $k_z = -k_z^{W(-)}$, the surface state is incorporated

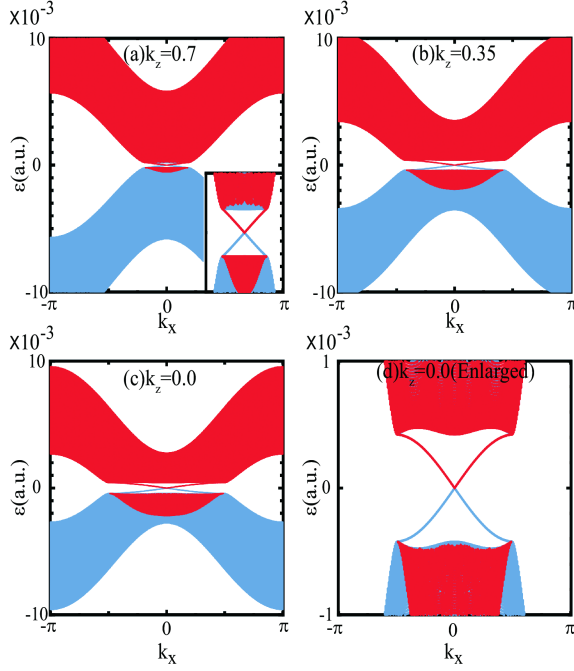


FIG. 4. Projected energy dispersions $\mathcal{E}(\bar{\mathbf{k}})$ with a surface state of down-spin. The axis of abscissa k_x is gauged in the unit of $1/d_x$. Here, bands dominated rather by the s/p -orbital component are denoted by a red/blue solid line. (a) $\mathcal{E}(\bar{\mathbf{k}})$ at $k_z = 0.7$ slightly smaller than $k_z^{W(-)}$. (b) The same as pannel (a) but at $k_z = 0.35$. (c) The same as pannel (a) but at $k_z = 0$. (d) Enlarged view of pannel (c).

with another surface Weyl point at $-\bar{\mathbf{k}}^{W(-)}$; though not shown here. These nontrivial surface states sliced in the interval $-k_z^{W(-)} \leq k_z \leq k_z^{W(-)}$ are unified to form a tilted surface band in the $k_x - k_z$ plane. Both edges of it are pinned to the respective surface Weyl points at $\pm \bar{\mathbf{k}}^{W(-)}$. This surface band is schematically depicted as the tilted surface that is colored blue in the right figure of Fig. 1(b).

Figures 5(a)-5(c) show the projected energy dispersions of up-spin bands with surface states at three different k_z 's. It is seen that the pattern of variance of the surface states formed here follows that shown in the down-spin bands of Fig. 4. However, the energy gap $\mathcal{E}_g^{(+)}$ is extremely smaller than $\mathcal{E}_g^{(-)}$, and as seen in Fig. 5(d), the surface band is slightly tilted with overall negative gradient and undulation. The pattern of variance in the negative k_z -direction is also subject to that seen in the down-spin bands; though not shown here. As a result, the nontrivial surface states sliced in the interval $-k_z^{W(+)} \leq k_z \leq k_z^{W(+)}$ form a slightly tilted and undulated surface band in the $k_x - k_z$ plane. Both edges of it are pinned to the respective surface Weyl points at $\pm \bar{\mathbf{k}}^{W(+)}$. This surface band is schematically depicted as the tilted surface that is colored red in the left figure of Fig. 1(b).

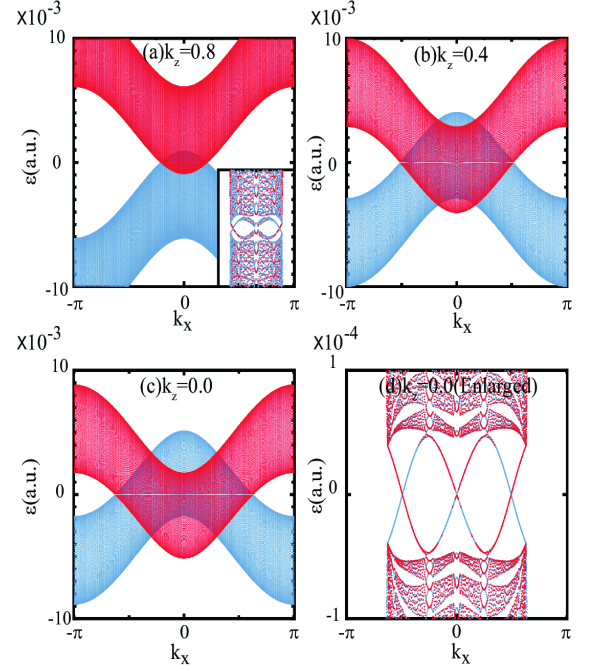


FIG. 5. Projected energy dispersions $\mathcal{E}(\bar{\mathbf{k}})$ with a surface state of up-spin. The axis of abscissa k_x is gauged in the unit of $1/d_x$. Here, bands dominated rather by the s/p -orbital component are denoted by a red/blue solid line. (a) $\mathcal{E}(\bar{\mathbf{k}})$ at $k_z = 0.8$ slightly smaller than $k_z^{W(+)}$. (b) The same as pannel (a) but at $k_z = 0.4$. (c) The same as pannel (a) but at $k_z = 0$. (d) Enlarged view of pannel (c).

D. Physical Properties

First, discussion is made on the chirality of the FWSM phases and the related topological phase transitions. It is considered that based on the qualitative discussion in Sec. III A, the conditions of generating the Weyl nodes for the up-spin and down-spin states are approximately evaluated as Eqs. (37) and (33), respectively. According to these, when ω is made greater from $\omega_1^{W(\pm)}$ and eventually identical to $\omega_2^{W(\pm)}$, the Weyl nodes at $\mathbf{k}^{W(\pm)}$ move along k_z axis from the Γ point $k_z = 0$ toward the boundary of the BZ at $k_z = \pi/d_z$ to annihilate with the other pair of the Weyl nodes at $-\mathbf{k}^{W(\pm)}$ that move in the opposite direction toward the boundary at $k_z = -\pi/d_z$; a double sign corresponds. This implies that the Weyl nodes at $\mathbf{k}^{W(\pm)}$ possess opposite handedness from that at the other Weyl nodes at $-\mathbf{k}^{W(\pm)}$. In other words, there should be the relations that

$$h_+^{(+)}h_-^{(+)} = -1, h_+^{(-)}h_-^{(-)} = -1, \quad (46)$$

where $h_{\pm}^{(+)}$ and $h_{\pm}^{(-)}$, which are either 1 or -1, represent helicities of the Weyl cones at $\pm \mathbf{k}^{W(+)}$ for the up-spin and $\pm \mathbf{k}^{W(-)}$ for the down-spin, respectively. Further, it is noted that the handedness of the Weyl node for the

up-spin state at $\mathbf{k}^{W(+)}(-\mathbf{k}^{W(+)})$ is opposite from that for the down-spin state at $\mathbf{k}^{W(-)}(-\mathbf{k}^{W(-)})$, because a pair of Weyl nodes for the up-spin and down-spin states at $\mathbf{k}^{W(+)}$ and $\mathbf{k}^{W(-)}$, respectively, are generated by splitting of the Dirac node at $\mathbf{k}^D(-\mathbf{k}^D)$ due to the breaking of the T-symmetry. That is, there should be the relations that

$$h_+^{(+)}h_+^{(-)} = -1, h_-^{(+)}h_-^{(-)} = -1. \quad (47)$$

Actually, the above relations of Eqs. (46) and (47) are confirmed by defining these helicities as Eqs. (B64) and (B69), followed by mathematical evaluation, as developed in Appendix B 4. Here, these expressions of helicities are extracted from effective Fourier-Weyl Hamiltonians of Eqs. (B61) and (B66), which are reduced from the original Floquet Hamiltonian of Eq. (12). Here, one mentions that recently, dynamical characterization of Floquet-Weyl nodes is discussed in Ref. 71.

In passing, when ω exceeds $\omega_2^{W(\pm)}$, the topological order is changed from the FWSM phase to a phase of Floquet topological insulator due to the gap opening. Further, the reduction of ω below $\omega_1^{W(\pm)}$ in the other direction brings the FWSM phase just back to a trivial insulator phase.

Figure 6 shows the energy dispersions $E^{(\pm)}(\mathbf{k})$ of up-spin and down-spin bands as a function of k_z with $k_x = k_y = 0$ for $\omega = 0.2 \sim 0.7$ eV. Below, discussion is made on the alteration of just $e(-1)$ and $hh(1)$ bands of an up-spin state (depicted by blue solid lines) and a down-spin state (depicted by red solid lines) with respect to ω . In the panel (a) for $\omega = 0.2$ eV, both spin bands are not inverted, and in the panel (b) for $\omega = 0.3$ eV, the up-spin band is inverted to form a FWSM phase with a pair of Floquet-Weyl nodes while the down-spin band is left open. In the panel (c) for $\omega = 0.35$ eV, both bands become inverted to form FWSM phases with two pairs of Floquet-Weyl nodes, and similarly, in the panel (d) for $\omega = 0.4$ eV ($< E_g$), both bands remain inverted. Such band inversion is still retained in the panels (e) and (f) even for $\omega = 0.5$ and 0.7 eV ($> E_g$). Incidentally, the discontinuities of the down-spin band seen in the panels (e) and (f) are due to an anticrossing between $e(-1)$ and $hh(0)$ and that between $e(0)$ and $hh(1)$. It is worth comparing these numerical results with the results estimated by Eqs. (37) and (33) based on the analytic model in Sec. III A, where $\omega_1^{W(+)} = 0.23$ eV, $\omega_2^{W(+)} = 0.64$ eV, $\omega_1^{W(-)} = 0.33$ eV, and $\omega_2^{W(-)} = 0.67$ eV. It is found that aside from the panel (f), the above-stated changes of topological order with respect to ω are well consistent with these estimated existence conditions of FWSM phases. The variance seen in the panel (f) is due to the breaking of the rotational-wave approximation adopted in this model. Actually, this approximation is considered accurate under the situation that $\omega \approx E_g (= 0.46$ eV).

Second, discussion is made on a magnetic property induced by the irradiation of the intense laser with a left-hand circular polarization. As far as the nearly resonant

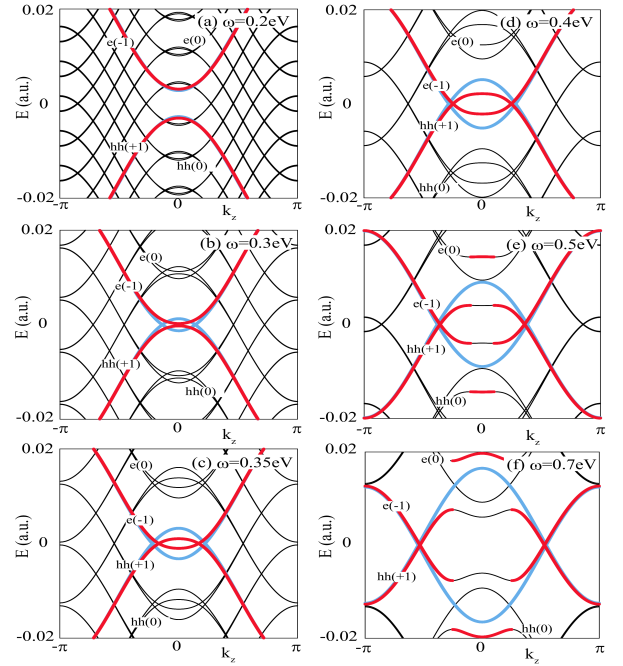


FIG. 6. Frequency dependence of energy dispersions $E^{(\pm)}(\mathbf{k})$ of up-spin and down-spin bands as a function of k_z with $k_x = k_y = 0$ for ω equal to (a) 0.2 eV (7.35×10^{-3} a.u.), (b) 0.3 eV (1.10×10^{-2} a.u.), (c) 0.35 eV (1.29×10^{-2} a.u.), (d) 0.4 eV (1.47×10^{-2} a.u.), (e) 0.5 eV (1.84×10^{-2} a.u.), and (f) 0.7 eV (2.57×10^{-2} a.u.). The abscissa k_z is gauged in the unit of $1/d_z$. The panel (d) is the same as Figs. 3(e) and 3(f). Here, the legend of ordinate $E^{(\pm)}(\mathbf{k})$ is simply represented as E . The up-spin bands $e(-1)$ and $hh(1)$ are depicted by blue solid lines, and the down-spin bands $e(-1)$ and $hh(1)$ are depicted by red solid lines. The parent bands are also labeled as $e(0)$ and $hh(0)$. In all panels, red solid lines are partially superimposed on blue solid lines.

optical transition is concerned, down-spin electrons that are situated in a valence band before the irradiation are selectively excited to a conduction band, and some fractions of the excited electrons are deexcited back to the valence band due to the Rabi oscillation, whereas up-spin electrons remain almost in the valence band; consult Sec. II B. In terms of the Floquet picture, these excitation and deexcitation processes in a series of the non-equilibrium dynamics are interpreted as couplings between one pair of down-spin bands $hh(1)$ and $e(0)$, and between another pair of down-spin bands $hh(0)$ and $e(-1)$, respectively. Thus, carriers are likely distributed to both bands of $e(-1)$ and $hh(1)$, which are further coupled by the two-photon interaction mentioned in Sec. III B to form the FWSM phase through the ac-Stark splitting. On the contrary, it is considered that the up-spin bands of $e(-1)$ and $hh(1)$ are almost unoccupied. Therefore, the down-spin electrons are exclusively distributed over the surface, while these coexist with the up-spin electrons in the bulk though both electronic states are energetically

separated by the amount of $\mathcal{E}_g^{(-)}$.

This implies that the system of concern exhibits transient surface magnetization with down spins that survives for as long as the associated population relaxation time, besides bulk magnetization that is expected to be induced as well. In addition with such an effect of spin magnetization, it is likely that the circularly polarized laser induces the inverse Faraday effect, which is a sort of a generation mechanism of orbital magnetization.^{98–102} This effect is expected to contribute the above surface magnetization to a certain extent. Indeed, the surface magnetization seems faint and transient, but the magnitude of it can be somewhat enhanced by increasing the strength of the circularly polarized laser. Moreover, the measurement of such an intriguing phenomenon would be feasible by means of the longitudinal magneto-optic Kerr effect that can detect the degree of strength of magnetization manifested just in the surface.^{107–109} To do this, a pump-probe measurement is expected to be effective, in which a linear polarized laser causing the magneto-optic Kerr effect is incorporated as a probe in addition with the pump laser with the left-hand circular polarization.

Below, additional comments on the results described in Secs III A–III C are enumerated.

(1) The up-spin FWSM band is considered as a FNLSM phase, because the band gap of $\mathcal{E}_g^{(+)}$ is of the order of 2 meV; consult Sec III B. Actually, such small energy separation and the concomitant surface state would be possibly smeared with homogeneous broadening due to an electron correlation effect and inhomogeneous broadening due to finite temporal width of a laser pulse — in place of the ideal continuous-wave laser —, which is of the order of a couple of meV for a pico-second pulse. Although the up-spin bands are almost unoccupied as stated above, these would be detectable by reconstructing the optical system of concern as follows: the up-spin bands of $e(-1)$ and $hh(1)$ are excited in advance by an intense ultrashort pulse laser with linear polarization, followed by the irradiation of the pico-second pulse (the continuous-wave laser) with the left-hand circular polarization.

(2) In view of the above comment (1), the surface states hosted by the down-spin band are entirely embedded in the continuum (bulk) of the FNLSM phase of the up-spin band; consult Figs. 4 and 5. When a spin flip interaction attributed to the spin-orbit coupling is tuned on, the surface states become somewhat unstable due to the effect of Fano resonance, namely, the collapse of the discrete levels of the surface states into the continuum states which is caused by the interaction between both of these states.¹¹⁰ The spin flip interaction becomes effective when either $d_1(\mathbf{k})$ or $d_2(\mathbf{k})$ has a non-negligible contribution to the effective Hamiltonian given in Eq. (6).

(3) The crystal Zn_3As_2 has a bulk rotational symmetry around the z -axis, and this leads to the formation of FWSMs under the conditions of Eqs. (33) and (37). In fact, there remains internal compression normal to this axis within the crystal, and this symmetry is considered

partially broken. Such breaking will open up a slight gap to make the Floquet system of concern insulating.⁷

IV. CONCLUSIONS

It is found that the narrow gap semiconductor Zn_3As_2 is driven by a left-hand circularly-polarized continuous-wave laser with frequency nearly resonant with the band gap E_g to produce the two types of FWSM phases simultaneously in the crystal, which are sharply distinguished by their spins. The bulk rotational symmetry around the z -axis protects a pair of Weyl nodes with opposite chirality along the k_z -axis in the respective FWSM phases under the condition of either Eq. (33) or Eq. (37). In the down-spin FWSM phase, the Floquet bands of $e(-1)$ and $hh(1)$ touch in a linear manner in the vicinity of the Weyl nodes situated at $\pm \mathbf{k}^{W(-)}$, hosting the nontrivial surface states pinned to both nodes. Since the above-mentioned laser makes electrons excited exclusively in the down-spin Floquet bands, it is considered that the surface states are selectively occupied by such spin-polarized electrons, showing transient magnetization with partial modification by the inverse Faraday effect. This surface magnetization would be measured by virtue of the magneto-optic Kerr effect. On the other hand, in the up-spin FWSM phase, the Floquet bands of $e(-1)$ and $hh(1)$ touch in the vicinity of the Weyl nodes situated at $\pm \mathbf{k}^{W(+)}$ almost in a quadratic manner in the k_x - and k_y -directions and in a linear manner in the k_z -direction. Because of the negligibly small band gap, this up-spin FWSM phase is rather considered as the FNLSM phase. To detect this phase somehow or other, it would be necessary to make excited electrons occupied in the up-spin bands in advance prior to the irradiation of the circularly polarized laser. The exploration of the transient non-equilibrium dynamics of the concerned system is inevitable in addition with Floquet band structures to deepen the understandings of the underlying physics of the FWSMs.

ACKNOWLEDGMENTS

This work was supported by JSPS KAKENHI Grant No. JP19K03695. The authors are grateful to Prof. J. Fujioka for fruitful comments and discussion.

Appendix A: Explicit expressions of

$$\tilde{D}_{j,nn'}(\mathbf{k}, \omega) \quad (j = 3 \sim 5) \text{ and } \tilde{V}_{nn'}^{(\pm)}$$

The Floquet matrix element $\tilde{D}_{j,nn'}(\mathbf{k}, \omega)$ seen in Eq. (12) is given by

$$\tilde{D}_{j,nn'}(\mathbf{k}, \omega) = \frac{1}{T} \int_0^T dt e^{-i\Delta n \omega t} D_j(\mathbf{k}, t) \quad (\text{A1})$$

with $\Delta n = n - n'$. This is expressed in terms of the N th-order Bessel function of the first kind

$$J_N(z_l) = \frac{1}{2\pi} \int_0^{2\pi} d\theta e^{-iN\theta} e^{iz_l \sin \theta} \quad (\text{A2})$$

with $z_l = F_l d_l / \omega$ ($l = x, y$) as follows:

$$\tilde{D}_{3,nn'}(\mathbf{k}, \omega) = \begin{cases} t_{sp} J_{\Delta n}(z_x) \sin(k_x d_x) & \text{for } \Delta n = 0, \pm 2, \pm 4, \dots \\ it_{sp} J_{\Delta n}(z_x) \cos(k_x d_x) & \text{for } \Delta n = \pm 1, \pm 3, \dots \end{cases} \quad (\text{A3})$$

$$\begin{aligned} \tilde{D}_{4,nn'}(\mathbf{k}, \omega) &= \begin{cases} \Delta_g - \sum_{l=x,y} 2t^{xy} [1 - J_0(z_l) \cos(k_l d_l)] - 2t^z [1 - \cos(k_z d_z)] & \text{for } \Delta n = 0 \\ 2t^{xy} [J_{\Delta n}(z_x) \cos(k_x d_x) + J_{\Delta n}(z_y) \cos(k_y d_y + \frac{\Delta n}{2}\pi)] & \text{for } \Delta n = \pm 2, \pm 4, \dots \\ 2t^{xy} [-iJ_{\Delta n}(z_x) \sin(k_x d_x) + J_{\Delta n}(z_y) \cos(k_y d_y + \frac{\Delta n}{2}\pi)] & \text{for } \Delta n = \pm 1, \pm 3, \dots \end{cases} \end{aligned} \quad (\text{A4})$$

and

$$\tilde{D}_{5,nn'}(\mathbf{k}, \omega) = \begin{cases} i^{\Delta n} t_{sp} J_{\Delta n}(z_y) \sin(k_y d_y) & \text{for } \Delta n = 0, \pm 2, \pm 4, \dots \\ i^{(\Delta n-1)} t_{sp} J_{\Delta n}(z_y) \cos(k_y d_y) & \text{for } \Delta n = \pm 1, \pm 3, \dots \end{cases} \quad (\text{A5})$$

Further, the Fourier transform of the electric-dipole interaction $V^{(\pm)}(t)$ of Eq. (16), given by

$$\tilde{V}_{nn'}^{(\pm)} = \frac{1}{T} \int_0^T dt e^{-i\Delta n \omega t} V^{(\pm)}(t), \quad (\text{A6})$$

is cast into

$$\tilde{V}_{nn'}^{(\pm)} = \begin{pmatrix} 0 & \frac{1}{2i}(\Omega_y \pm \Omega_x)\delta_{n,n'+1} \\ -\frac{1}{2i}(\Omega_y \mp \Omega_x)\delta_{n,n'-1} & 0 \end{pmatrix}. \quad (\text{A7})$$

Appendix B: Analytic expressions of energy dispersion $E(\mathbf{k})$

1. Floquet Hamiltonian and approximate eigenvalues

The eigenvalue problem of the following Floquet Hamiltonian for up- and down-spins

$$L^{(\pm)}(\mathbf{k}, t) = H^{(\pm)}(\mathbf{k}, t) + V^{(\pm)}(t) - iI_2 \frac{\partial}{\partial t} \quad (\text{B1})$$

is solved approximately to obtain analytic expressions of eigenvalue $E(\mathbf{k})$, where $H^{(\pm)}(\mathbf{k}, t)$ and $V^{(\pm)}(t)$ are

given in Eqs. (18) and (16), respectively. The associated Fourier-Floquet matrix $\tilde{L}^{(\pm)}(\mathbf{k}, \omega)$ is represented as

$$\tilde{L}^{(\pm)}(\mathbf{k}, \omega) = \begin{pmatrix} \ddots & \vdots & \vdots & \ddots \\ \cdots & \mathcal{L}_{n,n}^{(\pm)} & \mathcal{X}_{n,n-1}^{(\pm)} & \cdots \\ \cdots & \mathcal{X}_{n-1,n}^{(\pm)} & \mathcal{L}_{n-1,n-1}^{(\pm)} & \cdots \\ \ddots & \vdots & \vdots & \ddots \end{pmatrix} \quad (\text{B2})$$

where $\mathcal{L}_{n,n}^{(\pm)}$ and $\mathcal{X}_{n,n-1}^{(\pm)}$ are 2×2 -block-matrices defined by

$$\mathcal{L}_{n,n}^{(\pm)} = \begin{pmatrix} \tilde{L}_{1(n)1(n)}^{(\pm)} & \tilde{L}_{1(n)2(n+1)}^{(\pm)} \\ \tilde{L}_{2(n+1)1(n)}^{(\pm)} & \tilde{L}_{2(n+1)2(n+1)}^{(\pm)} \end{pmatrix} \quad (\text{B3})$$

and

$$\mathcal{X}_{n,n-1}^{(\pm)} = \begin{pmatrix} \tilde{L}_{1(n)1(n-1)}^{(\pm)} & \tilde{L}_{1(n)2(n)}^{(\pm)} \\ \tilde{L}_{2(n+1)1(n-1)}^{(\pm)} & \tilde{L}_{2(n+1)2(n)}^{(\pm)} \end{pmatrix} \quad (\text{B4})$$

with $\mathcal{X}_{n-1,n}^{(\pm)} = [\mathcal{X}_{n,n-1}^{(\pm)}]^\dagger$, respectively. Here, $\tilde{L}_{b(n)b'(n')}$ is a Fourier-transform of the (b, b') -matrix element of $L^{(\pm)}(\mathbf{k}, t)$, that is,

$$\tilde{L}_{b(n)b'(n')}^{(\pm)} = \frac{1}{T} \int_0^T dt e^{-i\Delta n \omega t} L_{bb'}^{(\pm)}(\mathbf{k}, t), \quad (\text{B5})$$

where it is understood that the index $b = 1(2)$ represents the conduction (valence) band.

Now, an approximation is made that $\tilde{L}^{(\pm)}(\mathbf{k}, \omega)$ is replaced by a sequence of 4×4 -block matrices $\{L_n^{(\pm)}\}$,

$$\tilde{L}^{(\pm)}(\mathbf{k}, \omega) \approx \begin{pmatrix} \ddots & & & \\ & L_{n+1}^{(\pm)} & O & \\ & {}^tO & L_n^{(\pm)} & \\ & & & L_{n-1}^{(\pm)} \\ & & & & \ddots \end{pmatrix}, \quad (\text{B6})$$

where the off-diagonal elements are represented in terms of a null upper-triangular block O and its transpose tO , and the diagonal block matrix is given by

$$L_n^{(\pm)} = \begin{pmatrix} \mathcal{L}_{n,n}^{(\pm)} & \mathcal{X}_{n,n-1}^{(\pm)} \\ \mathcal{X}_{n-1,n}^{(\pm)} & \mathcal{L}_{n-1,n-1}^{(\pm)} \end{pmatrix}. \quad (\text{B7})$$

It is obvious that this corresponds to the rotational-wave approximation, in which just almost resonant coupling terms of $\mathcal{X}_{n,n-1}^{(\pm)}$ and $\mathcal{X}_{n-1,n}^{(\pm)}$ are sustained, and the rest terms are disregarded. In Eq. (B3), the diagonal elements of $\tilde{L}_{1(n)1(n)}^{(\pm)}$ and $\tilde{L}_{2(n+1)2(n+1)}^{(\pm)}$ of $\mathcal{L}_{n,n}^{(\pm)}$ are strongly coupled by the off-diagonal element, $\tilde{L}_{1(n)2(n+1)}^{(\pm)}$ and $\tilde{L}_{2(n+1)1(n)}^{(\pm)}$ representing interband interactions, when an almost on-resonant condition is met. Setting a set of

eigenvalues and the associated eigenvectors of $\mathcal{L}_{n,n}^{(\pm)}$ as $\mathcal{E}_{n,\alpha}^{(\pm)}$ and $u_{n,\alpha}^{(\pm)}$ with $\alpha = 1, 2$, respectively, that is,

$$\mathcal{L}_{n,n}^{(\pm)} u_{n,\alpha}^{(\pm)} = \mathcal{E}_{n,\alpha}^{(\pm)} u_{n,\alpha}^{(\pm)}, \quad (\text{B8})$$

with $U_n^{(\pm)}$ as a 2×2 -unitary matrix given by

$$U_n^{(\pm)} = \begin{pmatrix} u_{n,1}^{(\pm)} & u_{n,2}^{(\pm)} \end{pmatrix}, \quad (\text{B9})$$

$\bar{L}_n^{(\pm)}$ defined as

$$\bar{L}_n^{(\pm)} = U_n^{(\pm)\dagger} L_n^{(\pm)} U_n^{(\pm)} \quad (\text{B10})$$

becomes of the form

$$\begin{aligned} \bar{L}_n^{(\pm)} &= \begin{pmatrix} \mathcal{E}_n^{(\pm)} & \bar{\mathcal{X}}_{n,n-1}^{(\pm)} \\ \bar{\mathcal{X}}_{n-1,n}^{(\pm)} & \mathcal{E}_{n-1}^{(\pm)} \end{pmatrix} \\ &= \begin{pmatrix} \mathcal{E}_{n,1}^{(\pm)} & 0 & \times & \times \\ 0 & \mathcal{E}_{n,2}^{(\pm)} & \mathcal{V}^{(\pm)} & \times \\ \times & \mathcal{V}^{(\pm)*} & \mathcal{E}_{n-1,1}^{(\pm)} & 0 \\ \times & \times & 0 & \mathcal{E}_{n-1,2}^{(\pm)} \end{pmatrix}, \quad (\text{B11}) \end{aligned}$$

where

$$\mathcal{E}_n^{(\pm)} = \begin{pmatrix} \mathcal{E}_{n,1}^{(\pm)} & 0 \\ 0 & \mathcal{E}_{n,2}^{(\pm)} \end{pmatrix} \quad (\text{B12})$$

and

$$\bar{\mathcal{X}}_{n,n-1}^{(\pm)} = U_n^{(\pm)\dagger} \mathcal{X}_{n,n-1}^{(\pm)} U_{n-1}^{(\pm)} \equiv \begin{pmatrix} \times & \times \\ \mathcal{V}^{(\pm)} & \times \end{pmatrix}. \quad (\text{B13})$$

In the second equality of the above equation, $\mathcal{V}^{(\pm)}$ represents the (2,1)-components of $\bar{\mathcal{X}}_{n,n-1}^{(\pm)}$ and all other components are expressed just as a symbol \times ; $\mathcal{V}^{(\pm)}$ is independent of n , as shown later. Here, it is supposed that just the component $\mathcal{V}^{(\pm)}$ is retained with neglecting the components denoted as \times .

Thus, one obtains two kinds of eigenenergies from Eq. (B11), — denoted as $E_{n,\beta}^{(\pm)}(\mathbf{k})$ with $\beta = 1, 2$ —, which are the eigenvalues of the 2×2 -block matrix

$$\bar{L}_{D,n}^{(\pm)} \equiv \begin{pmatrix} \mathcal{E}_{n,2}^{(\pm)} & \mathcal{V}^{(\pm)} \\ \mathcal{V}^{(\pm)*} & \mathcal{E}_{n-1,1}^{(\pm)} \end{pmatrix}. \quad (\text{B14})$$

Explicit expressions of $E_{n,\beta}^{(\pm)}$ are provided as

$$\begin{aligned} E_{n,\beta}^{(\pm)}(\mathbf{k}) &= \frac{1}{2} \left[\mathcal{E}_{n,2}^{(\pm)} + \mathcal{E}_{n-1,1}^{(\pm)} - (-1)^\beta \right. \\ &\quad \left. \times \sqrt{\left(\mathcal{E}_{n,2}^{(\pm)} - \mathcal{E}_{n-1,1}^{(\pm)} \right)^2 + 4|\mathcal{V}^{(\pm)}|^2} \right] \end{aligned} \quad (\text{B15})$$

Therefore, the approximate eigenvalues of $\tilde{L}^{(\pm)}(\mathbf{k}, \omega)$ of Eq. (B6) are given in terms of a series of the set of eigenvalues $\{E_{n,1}^{(\pm)}(\mathbf{k}), E_{n,2}^{(\pm)}(\mathbf{k})\}$.

2. Energy dispersions of FWSM states

The more detailed expressions of $E_{n,\beta}^{(\pm)}(\mathbf{k})$ are sought. To do this, $\mathcal{E}_{n,\alpha}^{(\pm)}$ is represented in terms of the matrix elements of Eq. (B3) as

$$\mathcal{E}_{n,\alpha}^{(\pm)} = \frac{1}{2} \left[\epsilon_n^{0(\pm)} - (-1)^\alpha \sqrt{\left(\Delta \epsilon_n^{(\pm)} \right)^2 + 4|\mathcal{W}^{(\pm)}|^2} \right], \quad (\text{B16})$$

where

$$\epsilon_n^{0(\pm)} = \tilde{L}_{1(n)1(n)}^{(\pm)} + \tilde{L}_{2(n+1)2(n+1)}^{(\pm)}, \quad (\text{B17})$$

$$\Delta \epsilon_n^{(\pm)} = \tilde{L}_{1(n)1(n)}^{(\pm)} - \tilde{L}_{2(n+1)2(n+1)}^{(\pm)}, \quad (\text{B18})$$

and

$$\mathcal{W}^{(\pm)} = \tilde{L}_{1(n)2(n+1)}^{(\pm)}. \quad (\text{B19})$$

According to the explicit expressions of $\tilde{D}_{j,nn'}(\mathbf{k}, \omega)$ obtained in Appendix A, it is shown that

$$\epsilon_n^{0(\pm)} = (2n+1)\omega \quad (\text{B20})$$

and

$$\Delta \epsilon_n^{(\pm)} \equiv 2\eta(\mathbf{k}) = 2D(\mathbf{k}) - \omega, \quad (\text{B21})$$

where

$$\begin{aligned} D(\mathbf{k}) &= \Delta_g + \epsilon_z(k_z) \\ &\quad - \sum_{l=x,y} 2t^{xy} [1 - J_0(z_l) \cos(k_l d_l)], \end{aligned} \quad (\text{B22})$$

with

$$\epsilon_z(k_z) = -2t^z [1 - \cos(k_z d_z)]. \quad (\text{B23})$$

Similarly, in view of $\tilde{V}_{nn'}^{(\pm)}$ given in Appendix A, one has

$$\begin{cases} \mathcal{W}^{(+)} = -\frac{i}{2}\Omega_x - it_{sp}J_1(z_x) \cos(k_x d_x) \\ \mathcal{W}^{(-)} = (\mathcal{W}^{(+)})^* \end{cases} \quad (\text{B24})$$

for the linearly polarized light, and

$$\begin{cases} \mathcal{W}^{(+)} = -it_{sp}J_1(z_c) [\cos(k_x d_x) + \cos(k_y d_y)] \\ \mathcal{W}^{(-)} = it_{sp}J_1(z_c) [\cos(k_x d_x) - \cos(k_y d_y)] \\ \quad + i\Omega_c \end{cases} \quad (\text{B25})$$

for the circularly polarized light, with $\Omega_c \equiv \Omega_x = \Omega_y$.

Further, $U_n^{(\pm)}$ of Eq. (B9) is given by

$$u_{n,1}^{(\pm)} = \begin{pmatrix} \cos \Theta^{(\pm)} \\ \sin \Theta^{(\pm)} e^{-i\Phi^{(\pm)}} \end{pmatrix} \quad (\text{B26})$$

and

$$u_{n,2}^{(\pm)} = \begin{pmatrix} \sin \Theta'^{(\pm)} e^{i\Phi'^{(\pm)}} \\ \cos \Theta'^{(\pm)} \end{pmatrix}, \quad (\text{B27})$$

where

$$\tan \Theta^{(\pm)} = \frac{|\mathcal{W}^{(\pm)}|}{\eta(\mathbf{k}) + \sqrt{\eta(\mathbf{k})^2 + |\mathcal{W}^{(\pm)}|^2}}, \quad (\text{B28})$$

$$\tan \Theta'^{(\pm)} = -\tan \Theta^{(\pm)}, \quad (\text{B29})$$

and

$$e^{i\Phi^{(\pm)}} = \frac{\mathcal{W}^{(\pm)}}{|\mathcal{W}^{(\pm)}|}. \quad (\text{B30})$$

Thus, $\mathcal{V}^{(\pm)}$ of Eq. (B13) is approximately given by

$$\mathcal{V}^{(\pm)} \approx \tilde{L}_{1(n)2(n)}^{(\pm)} \sin \Theta^{(\pm)} \sin \Theta'^{(\pm)} e^{-2i\Phi^{(\pm)}}, \quad (\text{B31})$$

where just the most dominant component $\tilde{L}_{1(n)2(n)}^{(\pm)}$ in $\mathcal{X}_{n,n-1}^{(\pm)}$ of Eq. (B4) is kept under the condition that $J_0(z_l) \gg J_{n(\geq 1)}(z_l)$ in the range of z_l concerned here. To be more specific, $\tilde{L}_{1(n)2(n)}^{(\pm)}$ is represented as

$$\tilde{L}_{1(n)2(n)}^{(\pm)} = \pm t_{sp} [J_0(z_x) \sin(k_x d_x) \mp i \sin(k_y d_y)] \quad (\text{B32})$$

for the the linearly polarized light, and

$$\tilde{L}_{1(n)2(n)}^{(\pm)} = \pm t_{sp} J_0(z_c) [\sin(k_x d_x) \mp i \sin(k_y d_y)] \quad (\text{B33})$$

for the the circularly polarized light.

According to the above results, $E_{n,\beta}^{(\pm)}(\mathbf{k})$ of Eq. (B15) is cast into

$$E_{n,\beta}^{(\pm)}(\mathbf{k}) = n\omega + E_{0,\beta}^{(\pm)}(\mathbf{k}), \quad (\text{B34})$$

where

$$E_{0,\beta}^{(\pm)}(\mathbf{k}) = (-1)^{\beta-1} \left[\left\{ \omega/2 - \left(\eta(\mathbf{k})^2 + |\mathcal{W}^{(\pm)}|^2 \right)^{1/2} \right\}^2 + |\mathcal{V}^{(\pm)}|^2 \right]^{1/2}. \quad (\text{B35})$$

Obviously, it is likely that these two photon sidebands, $E_{n,1}^{(\pm)}(\mathbf{k})$ and $E_{n',2}^{(\pm)}(\mathbf{k})$, touch each other when the following conditions are met: $n = n'$ and the expression inside the square brackets of Eq. (B35) vanishes. The second condition is ensured only when $k_x = k_y = 0$, that is, $\mathcal{V}^{(\pm)} = 0$. Thus, this becomes the existence condition of a touching point at $k_z^{D/W(\pm)}$ satisfying the relation

$$\epsilon_z(k_z^{D/W(\pm)}) = \omega/2 - \Delta'_g + \sqrt{(\omega/2)^2 - |\mathcal{W}_0^{(\pm)}|^2}, \quad (\text{B36})$$

where

$$\Delta'_g = \Delta_g - \sum_{l=x,y} 2t^{xy} [1 - J_0(z_l)] \quad (\text{B37})$$

and

$$\mathcal{W}_0^{(\pm)} = \mathcal{W}^{(\pm)}|_{k_x=k_y=0}. \quad (\text{B38})$$

Here, $k_z^{D(\pm)}$ represents a solution of Eq. (B36) for the drive of linearly polarized laser, while $k_z^{W(\pm)}$ for the drive of circularly polarized laser. In view of Eq. (B23), a certain pair of values, $k_z^{D/W(\pm)}$ and $-k_z^{D/W(\pm)}$, exists under the condition that

$$\begin{aligned} -\omega/2 + \Delta'_g &< \sqrt{(\omega/2)^2 - |\mathcal{W}_0^{(\pm)}|^2} \\ &< -\omega/2 + \Delta'_g - 4t^z \end{aligned} \quad (\text{B39})$$

with $t^z < 0$, and

$$\omega/2 > |\mathcal{W}_0^{(\pm)}|. \quad (\text{B40})$$

The above condition is recast into

$$\begin{aligned} \text{Max} \left(2|\mathcal{W}_0^{(\pm)}|, \frac{\Delta_g'^2 + |\mathcal{W}_0^{(\pm)}|^2}{\Delta_g'} \right) &< \omega \\ &< \frac{(\Delta_g' - 4t^z)^2 + |\mathcal{W}_0^{(\pm)}|^2}{\Delta_g' - 4t^z}. \end{aligned} \quad (\text{B41})$$

It is evident that these pairs of values $k_z^{D/W(\pm)}$ and $-k_z^{D/W(\pm)}$ correspond to nodal points lying on the $\Gamma - Z$ axis in the BZ for FDSM/FWSM states.

3. Band structures of $E_{hh(1)}^{(\pm)}(\mathbf{k}, \omega)$ and $E_{e(-1)}^{(\pm)}(\mathbf{k}, \omega)$

Here, the label $b(n)$ (with $b = e, hh$) is introduced to represent a Floquet state attributed to b -band with n photon dressing; e and hh mean electron and heavy-hole bands, respectively. Following this, a Floquet energy $E^{(\pm)}(\mathbf{k})$ is given by

$$E_{hh(n+1)}^{(\pm)}(\mathbf{k}) \equiv E_{n,1}^{(\pm)}(\mathbf{k}) \geq n\omega \quad (\text{B42})$$

and

$$E_{e(n-1)}^{(\pm)}(\mathbf{k}) \equiv E_{n,2}^{(\pm)}(\mathbf{k}) \leq n\omega \quad (\text{B43})$$

in the case that a Floquet band $hh(n+1)$ is located above a Floquet band $e(n-1)$. In the opposite case that $hh(n+1)$ is located below $e(n-1)$, it is understood that the above definition of $E_{hh(n+1)}^{(\pm)}(\mathbf{k})$ is replaced by that of $E_{e(n-1)}^{(\pm)}(\mathbf{k})$.

Below, an energy dispersion of $E^{(\pm)}(\mathbf{k}) = E_{hh(1)}^{(\pm)}(\mathbf{k}) \geq 0$ in the vicinity of $\mathbf{k}^{D/W(\pm)} \equiv (0, 0, k_z^{D/W(\pm)})$ is examined, where $E_{e(-1)}^{(\pm)}(\mathbf{k}) = -E_{hh(1)}^{(\pm)}(\mathbf{k})$. To do this, $\eta(\mathbf{k})$, $\mathcal{W}^{(\pm)}$, and $\mathcal{V}^{(\pm)}$ are expanded around this point as follows:

$$\begin{aligned} \eta(\mathbf{k}) &\approx \eta_0 + \eta_z^{(1)}(\Delta k_z d_z) \\ &\quad + \sum_{l=x,y} \eta_l(k_l d_l)^2 + \eta_z(\Delta k_z d_z)^2, \end{aligned} \quad (\text{B44})$$

$$\mathcal{W}^{(\pm)} \approx \mathcal{W}_0^{(\pm)} + \sum_{l=x,y} \omega_l^{(\pm)} (k_l d_l)^2, \quad (\text{B45})$$

and

$$\mathcal{V}^{(\pm)} \approx \sum_{l=x,y} \nu_l^{(\pm)} (k_l d_l), \quad (\text{B46})$$

where $\Delta k_z = k_z - k_z^{D/W(\pm)}$, and the expansion coefficients $\eta_0, \eta_z^{(1)}, \eta_l, \eta_z, \mathcal{W}_0^{(\pm)}, \omega_l^{(\pm)}$, and $\nu_l^{(\pm)}$ are represented by

$$\begin{aligned} \eta_0 &= \Delta'_g + \epsilon_z (k_z^{D/W(\pm)}) - \omega/2, \eta_z^{(1)} = -2t^z \sin(k_z^{D/W(\pm)} d_z), \\ \eta_l &\approx -t^{xy}, \eta_z = -t^z \cos(k_z^{D/W(\pm)} d_z), \end{aligned} \quad (\text{B47})$$

$$\begin{cases} \mathcal{W}_0^{(+)} = -\frac{i}{2}\Omega_x, & \mathcal{W}_0^{(-)} = \frac{i}{2}\Omega_x \quad (\text{linear}) \\ \mathcal{W}_0^{(+)} = 0, & \mathcal{W}_0^{(-)} = i\Omega_c \quad (\text{circular}) \end{cases}, \quad (\text{B48})$$

$$\omega_l^{(\pm)} \approx 0 \quad (\text{B49})$$

and

$$\nu_x^{(\pm)} = \pm \sigma^{(\pm)} t_{sp}, \quad \nu_y^{(\pm)} = -i \sigma^{(\pm)} t_{sp}, \quad (\text{B50})$$

respectively. It is considered that $J_0(z_l) \approx 1$ in the range of z_l concerned here in Eq. (B47), terms including $t_{sp} J_1(z_l)$ are neglected due to $|J_1(z_l)| \ll 1$ in Eqs. (B48) and (B49), and the prefactor $\sigma^{(\pm)}$ is given by

$$\sigma^{(\pm)} = \sin \Theta_0^{(\pm)} \sin \Theta_0'^{(\pm)} e^{-2i\Phi_0^{(\pm)}} \quad (\text{B51})$$

in Eq. (B50), where

$$\begin{aligned} \Theta_0^{(\pm)} &= \Theta^{(\pm)}|_{\mathbf{k}=\mathbf{k}^{D/W(\pm)}}, \quad \Theta_0'^{(\pm)} = \Theta'^{(\pm)}|_{\mathbf{k}=\mathbf{k}^{D/W(\pm)}}, \\ \Phi_0^{(\pm)} &= \Phi^{(\pm)}|_{\mathbf{k}=\mathbf{k}^{D/W(\pm)}}. \end{aligned} \quad (\text{B52})$$

For the FDSM driven by the linearly polarized light,

$$\begin{aligned} E^{(\pm)}(\mathbf{k}) &\approx \left[\sum_{l=x,y} \nu_l^{(\pm)} (k_l d_l) \right]^2 + \frac{(\eta_0 \eta_z^{(1)})^2}{(\omega/2)^2} (\Delta k_z d_z)^2 \Bigg]^{1/2} \\ &= \left[\sum_{l=x,y} (\xi_l^D)^2 (k_l d_l)^2 + (\xi_z^D)^2 (\Delta k_z d_z)^2 \right]^{1/2}, \end{aligned} \quad (\text{B53})$$

where $\Delta k_z = k_z - k_z^{D(\pm)}$, $\xi_x^D = \xi_y^D = |\sigma^{(\pm)}| t_{sp}$ with

$$|\sigma^{(\pm)}| = \frac{(\Omega_x/2)^2}{(\Omega_x/2)^2 + \left(\eta_0 + \sqrt{\eta_0^2 + (\Omega_x/2)^2} \right)^2}, \quad (\text{B54})$$

and $\xi_z^D = |\eta_0 \eta_z^{(1)}|/(\omega/2)$. Hence, it is seen that the Floquet bands of $E_{hh(1)}^{(\pm)}(\mathbf{k})$ and $E_{e(-1)}^{(\pm)}(\mathbf{k})$ cross linearly at the Dirac points of $\mathbf{k}^{D(\pm)}$ and $-\mathbf{k}^{D(\pm)}$. On the other

hand, for the FWSM driven by the circularly polarized light,

$$\begin{aligned} E^{(+)}(\mathbf{k}) &\approx \left| \sum_{l=x,y} \eta_l (k_l d_l)^2 + \eta_z^{(1)} (\Delta k_z d_z) + \eta_z (\Delta k_z d_z)^2 \right| \\ &= \left| (-t^{xy}) \sum_{l=x,y} (k_l d_l)^2 + \eta_z^{(1)} (\Delta k_z d_z) + \eta_z (\Delta k_z d_z)^2 \right|, \end{aligned} \quad (\text{B55})$$

due to $\mathcal{W}_0^{(+)} = 0$ and $\nu_x^{(+)} = i\nu_y^{(+)} = \sigma^{(+)} t_{sp} \approx 0$ with $|\sigma^{(+)}| = [t_{sp} J_1(z_c)/(2\eta_0)]^2$, where $\Delta k_z = k_z - k_z^{W(+)}$, while

$$\begin{aligned} E^{(-)}(\mathbf{k}) &\approx \left[\sum_{l=x,y} \nu_l^{(-)} (k_l d_l) \right]^2 + \frac{(\eta_0 \eta_z^{(1)})^2}{(\omega/2)^2} (\Delta k_z d_z)^2 \Bigg]^{1/2} \\ &= \left[\sum_{l=x,y} (\xi_l^W)^2 (k_l d_l)^2 + (\xi_z^W)^2 (\Delta k_z d_z)^2 \right]^{1/2}, \end{aligned} \quad (\text{B56})$$

where $\Delta k_z = k_z - k_z^{W(-)}$, $\xi_x^W = \xi_y^W = |\sigma^{(-)}| t_{sp}$ with

$$|\sigma^{(-)}| = \frac{(\Omega_c)^2}{(\Omega_c)^2 + \left(\eta_0 + \sqrt{\eta_0^2 + (\Omega_c)^2} \right)^2}, \quad (\text{B57})$$

and $\xi_z^W = |\eta_0 \eta_z^{(1)}|/(\omega/2)$. Hence, it is seen that the Floquet bands of $E_{hh(1)}^{(+)}(\mathbf{k})$ and $E_{e(-1)}^{(+)}(\mathbf{k})$ cross in a quadratic manner in the k_x - and k_y -directions and in a linear manner in the k_z -direction at the Weyl points of $\mathbf{k}^{W(+)}$ and $-\mathbf{k}^{W(+)}$. On the other hand, those of $E_{hh(1)}^{(-)}(\mathbf{k})$ and $E_{e(-1)}^{(-)}(\mathbf{k})$ cross in a linear manner at the Weyl points of $\mathbf{k}^{W(-)}$ and $-\mathbf{k}^{W(-)}$, similar to the FDSMs.

Finally, band structures in the vicinity of the $k_x - k_y$ plane with k_z fixed are examined. For the FWSM of the up-spin state, $E^{(+)}(\mathbf{k})$ is represented simply as

$$E^{(+)}(\mathbf{k}) \approx |\omega/2 - D(\mathbf{k})| \quad (\text{B58})$$

due to Eq. (B35), where $\mathcal{W}^{(+)}$ and $\mathcal{V}^{(+)}$ are neglected within the order of $t_{sp} J_1(z_c) \approx 0$. Thus, $E_{hh(1)}^{(+)}(\mathbf{k}) \approx 0$ for \mathbf{k} 's situated on the closed surface

$$\begin{aligned} -2t^{xy} \sum_{l=x,y} [1 - J_0(z_l) \cos(k_l d_l)] - 2t^z [1 - \cos(k_z d_z)] \\ = \omega - \Delta_g > 0. \end{aligned} \quad (\text{B59})$$

This shows that there exists a nodal ring in the $k_x - k_y$ plane, which is reminiscent of a NLSM phase in the FWSM of concern. As regards the FWSM of the down-spin state, $E_{hh(1)}^{(-)}(\mathbf{k})$ and $E_{e(-1)}^{(-)}(\mathbf{k})$ are gapped out

in the $k_x - k_y$ plane due to $\mathcal{V}^{(-)}$ that is not negligible. It is remarked that an accidental band crossing occurs between these two bands at high-symmetry points of $\mathbf{k}^* = (0, 0, 0), (0, \pm\pi/d_y, 0), (\pm\pi/d_x, 0, 0)$, and $(\pm\pi/d_x, \pm\pi/d_y, 0)$ at which $\mathcal{V}^{(-)} = 0$, only when the relation

$$\omega/2 = \sqrt{\eta(\mathbf{k}^*)^2 + \Omega_c^2} \quad (\text{B60})$$

is ensured. In passing, the similar result with that of the FWSM of the down-spin state is applied for the FDSMs.

4. Floquet-Weyl Hamiltonian and Chirality

Here, effective Floquet-Weyl Hamiltonians the eigenvalues of which are given by Eqs. (B55) and (B56) are derived from Eq. (B14) in the vicinity of the Weyl points $\mathbf{k}^{W(+)}$ and $\mathbf{k}^{W(-)}$. The Hamiltonian for the up-spin band, represented as $L_n^{W(+)} \equiv \bar{L}_{D,n}^{(+)}$, is cast into

$$\begin{aligned} L_n^{W(+)} &= n\omega + \begin{pmatrix} -\eta_z^{(1)}(\Delta k_z d_z) & \sum_{l=x,y} \nu_l^{(+)}(k_l d_l) \\ \sum_{l=x,y} \nu_l^{(+)*}(k_l d_l) & \eta_z^{(1)}(\Delta k_z d_z) \end{pmatrix} \\ &= n\omega + h_+^{(+)} \mathbf{p}^{(+)} \cdot \boldsymbol{\sigma}, \end{aligned} \quad (\text{B61})$$

where Eqs. (B16), (B44), (B45), and (B46) are used. Further, the effective momentum $\mathbf{p}^{(+)}$, defined in the right-handed system, is given by

$$\begin{aligned} p_l^{(+)} &= h_+^{(+)} \sum_{l'=x,y,z} v_{ll'}^{(+)}(k_{l'} - k_{l'}^{W(+)}) \\ &\equiv h_+^{(+)} \mathbf{v}_l^{(+)} \cdot (\mathbf{k} - \mathbf{k}^{W(+)}), \end{aligned} \quad (\text{B62})$$

where

$$\begin{cases} \mathbf{v}_x^{(+)} = (\nu_x^{(+)} d_x, 0, 0) \\ \mathbf{v}_y^{(+)} = (0, \nu_y^{(+)} d_y, 0) \\ \mathbf{v}_z^{(+)} = (0, 0, -\eta_z^{(1)} d_z) \end{cases} \quad (\text{B63})$$

and $h_+^{(+)}$ is a helicity of particle at the Weyl point $\mathbf{k}^{W(+)}$, defined by

$$h_+^{(+)} = \text{sgn}(\mathbf{v}_x^{(+)} \times \mathbf{v}_y^{(+)} \cdot \mathbf{v}_z^{(+)}), \quad (\text{B64})$$

which is either +1 or -1. Thus, the positive eigenvalue of Eq. (B61) for $n = 0$ is given by

$$\begin{aligned} E^{W(+)}(\mathbf{k}) &= \left| (\eta_z^{(1)})^2 (\Delta k_z d_z)^2 + \nu_x^{(+)^2} \sum_{l=x,y} (k_l d_l)^2 \right|^{1/2} \\ &\approx \left| \eta_z^{(1)} (\Delta k_z d_z) \right|, \end{aligned} \quad (\text{B65})$$

where in the second equality the fact that $\nu_x^{(+)} \approx 0$ is considered. This is identical to Eq. (B55) within the first order with respect to k_x, k_y , and Δk_z .

Similarly, the Hamiltonian for the down-spin band, represented as $L_n^{W(-)} \equiv \bar{L}_{D,n}^{(-)}$, is cast into

$$\begin{aligned} L_n^{W(-)} &= n\omega + \begin{pmatrix} -\frac{\eta_0 \eta_z^{(1)}}{(\omega/2)} (\Delta k_z d_z) & \sum_{l=x,y} \nu_l^{(-)}(k_l d_l) \\ \sum_{l=x,y} \nu_l^{(-)*}(k_l d_l) & \frac{\eta_0 \eta_z^{(1)}}{(\omega/2)} (\Delta k_z d_z) \end{pmatrix} \\ &= n\omega + h_+^{(-)} \mathbf{p}^{(-)} \cdot \boldsymbol{\sigma}. \end{aligned} \quad (\text{B66})$$

Here, the effective momentum $\mathbf{p}^{(-)}$, defined in the right-handed system, is given by

$$\begin{aligned} p_l^{(-)} &= h_+^{(-)} \sum_{l'=x,y,z} v_{ll'}^{(-)}(k_{l'} - k_{l'}^{W(-)}) \\ &\equiv h_+^{(-)} \mathbf{v}_l^{(-)} \cdot (\mathbf{k} - \mathbf{k}^{W(-)}), \end{aligned} \quad (\text{B67})$$

where

$$\begin{cases} \mathbf{v}_x^{(-)} = (\nu_x^{(-)} d_x, 0, 0) \\ \mathbf{v}_y^{(-)} = (0, -\nu_y^{(-)} d_y, 0) \\ \mathbf{v}_z^{(-)} = (0, 0, -\frac{\eta_0 \eta_z^{(1)}}{(\omega/2)} d_z) \end{cases} \quad (\text{B68})$$

and $h_+^{(-)}$ is a helicity of particle at the Weyl point $\mathbf{k}^{W(-)}$, defined by

$$h_+^{(-)} = \text{sgn}(\mathbf{v}_x^{(-)} \times \mathbf{v}_y^{(-)} \cdot \mathbf{v}_z^{(-)}), \quad (\text{B69})$$

which is either +1 or -1. It is obvious that the positive eigenvalue of Eq. (B66) for $n = 0$, $E^{W(-)}(\mathbf{k})$, is identical to Eq. (B56).

Finally, the chiralities of FWSMs for both up- and down-spins are examined. Let the helicities of the Weyl cones at $-\mathbf{k}^{W(+)}$ and $-\mathbf{k}^{W(-)}$ be represented as $h_-^{(+)}$ and $h_-^{(-)}$, respectively. It is evident that $h_+^{(+)} h_-^{(+)} = -1$ and $h_+^{(-)} h_-^{(-)} = -1$, since according to Eqs (B47) and (B50), the replacement of the nodal position at $\mathbf{k}^{W(\pm)}$ by that at $-\mathbf{k}^{W(\pm)}$ still keeps $\nu_x^{(\pm)}$ unaltered, whereas $\eta_z^{(1)}$ changes its sign; a double sign corresponds. Further, it is also seen that $h_+^{(+)} h_+^{(-)} = -1$ and $h_-^{(+)} h_-^{(-)} = -1$, since the sign of $\eta_z^{(1)}$ remains unaltered, whereas the sign of $\nu_\pm^{(+)}$ is different from that of $\nu_\pm^{(-)}$; a double sign corresponds. Therefore, it is verified that each of four pairs of the Weyl cones at $\pm \mathbf{k}^{W(+)}$, $\pm \mathbf{k}^{W(-)}$, $\mathbf{k}^{W(\pm)}$, and $-\mathbf{k}^{W(\pm)}$ possesses opposite chiralities.

Appendix C: Enlarged view of Figs. 3(a) and 3(b)

Energy dispersions shown in Figs. 3(a) and 3(b) are enlarged in Fig. 7 to make clearer the difference of band gaps between the up-spin and down-spin bands around $E = 0$.

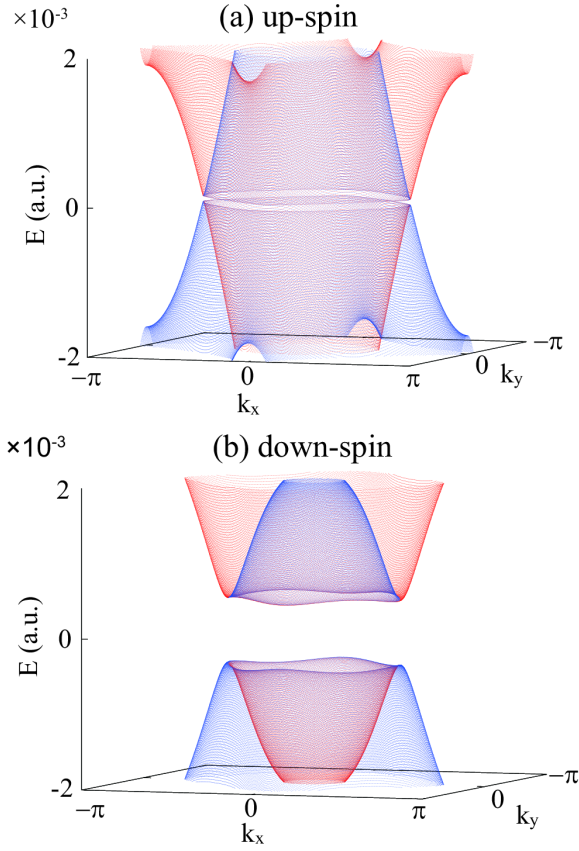


FIG. 7. Energy dispersions $E(\mathbf{k})$ of up-spin and down-spin bands at $k_z = 0$ which are enlarged around $E = 0$. Here, bands dominated rather by the s/p -orbital component are denoted by a red/blue solid line. The axis of abscissa k_l is gauged in the unit of $1/d_l$ with $l = x, y, z$. (a) $E(\mathbf{k})$ in the $k_x - k_y$ plane at $k_z = 0$ for the up-spin bands. (b) The same as panel (a) but for the down-spin bands.

* hino@ims.tsukuba.ac.jp

- ¹ C. L. Kane and E. J. Mele, Phys. Rev. Lett. **95**, 226801 (2005).
- ² B. A. Bernevig, T. L. Hughes, and S. C. Zhang, Science **314**, 1757 (2006).
- ³ M. Z. Hasan and C. L. Kane, Rev. Mod. Phys. **82**, 3045 (2010).
- ⁴ X. L. Qi and C. H. Zhang, Rev. Mod. Phys. **85**, 1057 (2011).
- ⁵ S. Murakami, S. Iso, Y. Avishai, M. Onoda, and N. Nagaosa, Phys. Rev. B **76**, 205304 (2007).
- ⁶ S. Murakami, New J. Phys. **9**, 356 (2007); Corrigendum. New J. Phys. **10**, 029802 (2008).
- ⁷ Z. Wang, Y. Sun, X. -Q. Chen, C. Franchini, G. Xu, H. Weng, X. Dai, and Z. Fang, Phys. Rev. B **85**, 195320 (2012).
- ⁸ Z. Wang, H. Weng, Q. Wu, X. Dai, and Z. Fang, Phys. Rev. B **88**, 125427 (2013).
- ⁹ S. M. Young, S. Zaheer, J. C.Y. Teo, C. L. Kane, E. J.

Mele, and A. M. Rappe, Phys. Rev. Lett. **108**, 140405 (2012).

- ¹⁰ S. M. Young and C. L. Kane, Phys. Rev. Lett. **115**, 126803 (2015).
- ¹¹ B. -J. Yang and N. Nagaosa, Nat. Comm. **5**, 4898 (2014).
- ¹² H. Yi, Z. Wang, C. Chen, Y. Shi, Y. Feng, A. Liang, Z. Xie, S. He, J. He, Y. Peng, X. Liu, Y. Liu, L. Zhao, G. Liu, X. Dong, J. Zhang, M. Nakatake, M. Arita, K. Shimada, H. Namatame, M. Taniguchi, Z. Xu, C. Chen, X. Dai, Z. Fang, and X. J. Zhou, Sci. Rep. **4**, 6106 (2014).
- ¹³ S.-Y. Xu, I. Belopolski, N. Alidoust, M. Neupane, G. Bian, C. Zhang, R. Sankar, G. Chang, Z. Yuan, C. -C. Lee, S. -M. Huang, H. Zheng, J. Ma, D. S. Sanchez, B. Wang, A. Bansil, F. Chou, P. P. Shibayev, H. Lin, S. Jia, and M. Z. Hasan, Science **349**, 613 (2015).
- ¹⁴ M. Kargarian, M. Randeria, and Y. -M. Lu, PNAS **113**, 8648 (2016).
- ¹⁵ S. Park and B. -J. Yang, Phys. Rev. B **96**, 125127 (2017).
- ¹⁶ H. Doh and H. J. Choi, 2D Mater. **4**, 025071 (2017).

- ¹⁷ B. Yan and C. Felser, *Annu. Rev. Condens. Matter Phys.* **8**, 337 (2017).
- ¹⁸ N. P. Armitage, E. J. Mele, and A. Vishwanath, *Rev. Mod. Phys.* **90**, 015001 (2018).
- ¹⁹ S. -Y. Yang, H. Yang, E. Derunova, S. S. P. Parkin, B. Yan, and M. N. Ali, *Advances in Physics: X*, **3**, 1414631 (2018).
- ²⁰ S. V. Ramankutty, J. Henke, A. Schiphorst, R. Nutakki, S. Bron, G. Araizi-Kanoutas, S. K. Mishra, L. Li, Y. Huang, T. K. Kim, M. Hoesch, C. Schlueter, T. -L. Lee, A. de Visser, Z. Zhong, J. van Wezel, E. van Heumen, and M. S. Golden, *SciPost Phys.* **4**, 010 (2018).
- ²¹ W. Luo, J. Ji, J. Lu, X. Zhang, and H. Xiang, *Phys. Rev. B* **101**, 195111 (2020).
- ²² F. K. Kunst, E. Edvardsson, J. C. Budich, and E. J. Bergholtz, *Phys. Rev. Lett.* **121**, 026808 (2018).
- ²³ S. Yao and Z. Wang, *Phys. Rev. Lett.* **121**, 086803 (2018).
- ²⁴ T. Ozawa, H. M. Price, A. Amo, N. Goldman, M. Hafezi, L. Lu, M. C. Rechtsman, D. Schuster, J. Simon, O. Zilberberg, and I. Carusotto, *Rev. Mod. Phys.* **91**, 015006 (2019).
- ²⁵ W. A. Benalcazar, B. A. Bernevig, and T. L. Hughes, *Science* **357**, 61 (2017).
- ²⁶ J. Langbehn, Y. Peng, L. Trifunovic, F. von Oppen, and P. W. Brouwer, *Phys. Rev. Lett.* **119**, 246401 (2017).
- ²⁷ Y. Peng, Y. Bao, and F. von Oppen, *Phys. Rev. B* **95**, 235143 (2017).
- ²⁸ J. C. Budich, B. Trauzettel, and P. Michetti, *Phys. Rev. Lett.* **112**, 146405 (2014).
- ²⁹ M. V. Entin, L. I. Magarill, and M. M. Mahmoodiana, *JETP Letters*, **103**, 328 (2016).
- ³⁰ K. Chen and R. Shindou, *Phys. Rev. B* **96**, 161101(R) (2017).
- ³¹ L. L. Li, and W. Xu, *Appl. Phys. Lett.* **104**, 111603 (2014).
- ³² Y. Deshko, L. Krusin-Elbaum, V. Menon, A. Khanikaev, and J. Trevino, *Optics Express* **24**, 7398 (2016).
- ³³ H. Weyl, *Z. Phys.* **56**, 330 (1929); *Proceedings of the National Academy of Sciences of the United States of America* **15**, 323 (1929).
- ³⁴ E. Majorana, *Nuovo Cimento* (1924-1942) **14**, 171 (1937).
- ³⁵ A. Gynther, K. Landsteiner, F. Pena-Benitez, and A. Rebhan, *J. High Energy Physics* **2011**, 110 (2011).
- ³⁶ S. R. Elliott and M. Franz, *Rev. Mod. Phys.* **87**, 137 (2015).
- ³⁷ S. L. Adler, *Phys. Rev.* **177**, 2426 (1969).
- ³⁸ J. S. Bell and R. Jackiw, *Nuovo Cimento A* **60**, 47 (1969).
- ³⁹ H. B. Nielsen and M. Ninomiya : *Phys. Lett. B* **130**, 389 (1983).
- ⁴⁰ D. T. Son and B. Z. Spivak, *Phys. Rev. B* **88**, 104412 (2013).
- ⁴¹ A. A. Burkov, *Phys. Rev. Lett.* **113**, 247203 (2014).
- ⁴² A. A. Burkov, *J. Phys.: CM.*, **27**, 113201 (2015).
- ⁴³ J. Xiong, S. K. Kushwaha, T. Liang, J. W. Krizan, M. Hirschberger, W. Wang, R. J. Cava, and N. P. Ong, *Science* **350**, 6259 (2015).
- ⁴⁴ S. Jeon, B. B. Zhou, A. Gyenis, B. E. Feldman, I. Kimchi, A. C. Potter, Q. D. Gibson, R. J. Cava, A. Vishwanath, and A. Yazdani, *Nat. Mater.* **13**, 851 (2014).
- ⁴⁵ J. Feng, Y. Pang, D. Wu, Z. Wang, H. Weng, J. Li, X. Dai, Z. Fang, Y. Shi, and L. Lu, *Phys. Rev. B* **92**, 081306 (2015).
- ⁴⁶ T. Liang, Q. Gibson, M. N. Ali, M. Liu, R. Cava, and N. Ong, *Nat. Mater.* **14**, 280 (2015).
- ⁴⁷ L. X. Wang, C. -Z. Li, D. -P. Yu, and Z. -M. Liao, *Nat. Commun.* **7**, 10769 (2016).
- ⁴⁸ F. Arnold, C. Shekhar, S. -C. Wu, Y. Sun, R. D. Dos Reis, N. Kumar, M. Naumann, M. O. Ajeesh, M. Schmidt, A. G. Grushin, and J. H. Bardarson, *Nat. Commun.* **7**, 11615 (2016).
- ⁴⁹ X. Huang, L. Zhao, Y. Long, P. Wang, D. Chen, Z. Yang, H. Liang, M. Xue, H. Weng, Z. Fang, and X. Dai, *Phys. Rev. X* **5**, 031023 (2015).
- ⁵⁰ M. Ali, J. Xiong, S. Flynn, J. Tao, Q. Gibson, L. Schoop, T. Liang, N. Haldolaarachchige, M. Hirschberger, N. Ong, and R. Cava, *Nature* **514**, 205 (2014).
- ⁵¹ C. Shekhar, A. K. Nayak, Y. Sun, M. Schmidt, M. Nicklas, I. Leermakers, U. Zeitler, Y. Skourski, J. Wosnitza, Z. Liu, and Y. Chen, *Nat. Phys.* **11**, 645 (2015).
- ⁵² R. Wang, B. Wang, R. Shen, L. Sheng, D. Y. Xing, and S. Y. Savrasov, *EPL (Europhys. Lett.)* **105**, 17004 (2014).
- ⁵³ K. Taguchi, T. Imaeda, M. Sato, and Y. Tanaka, *Phys. Rev. B* **93**, 201202(R) (2016).
- ⁵⁴ K. Taguchi, D. -H. Xu, A. Yamakage, and K. T. Law, *Phys. Rev. B* **94**, 155206 (2016).
- ⁵⁵ H. Hübener, M. A. Sentef, U. De Giovannini, A. F. Kemper, and A. Rubio, *Nat. Comm.* **8**, 13940 (2016).
- ⁵⁶ Jin-Yu Zou and Bang-Gui Liu, *Phys. Rev. B* **93**, 205435 (2016).
- ⁵⁷ X. -X. Zhang¹, T. T. Ong, and N. Nagaosa, *Phys. Rev. B* **94**, 235137 (2016).
- ⁵⁸ R. Chen, B. Zhou, and D. -H. Xu, *Phys. Rev. B* **97**, 155152 (2018); *Erratum Phys. Rev. B* **100**, 049901 (2019).
- ⁵⁹ U. Kumar, *Mater. Res. Express* **6**, 096304 (2019).
- ⁶⁰ Y. Zhu , T. Qin, X. Yang , G. Xianlong, and Z. Liang, *Phys. Rev. Research* **2**, 033045 (2020).
- ⁶¹ G. Salerno , N. Goldman, and G. Palumbo, *Phys. Rev. Research* **2**, 013224 (2020).
- ⁶² Y. Gao, C. Wang, and D. Xiao, *arXiv:2009.13392 [cond-mat.mes-hall]*.
- ⁶³ M. Kawaguchi, H. Hirose, Z. Chi, Y. -C. Lau, F. Freimuth, and M. Hayashi, *arXiv:2009.01388 [cond-mat.mes-hall]*.
- ⁶⁴ I. D. Tokman, Q. Chen, I. A. Shereshevsky, V. I. Pozdnyakova, I. Oladyshkin, M. Tokman, and A. Belyanin, *Phys. Rev. B* **101**, 174429 (2020).
- ⁶⁵ B. Zhang, N. Maeshima, and K. Hino, *Sci. Rep.* **11**, 2952 (2021).
- ⁶⁶ L. Liang , P. O. Sukhachov, and A. V. Balatsky, *Phys. Rev. Lett.* **126**, 247202 (2021).
- ⁶⁷ J. Ma and D. A. Pesin, *Phys. Rev. B* **92**, 235205 (2015).
- ⁶⁸ F. de Juan, A. G. Grushin, T. Morimoto, and J. E. Moore, *Nat. Commun.* **8**, 15995 (2017).
- ⁶⁹ S. A. A. Ghorashi, P. Hosur, and C. -S. Ting, *Phys. Rev. B* **97**, 205402 (2018).
- ⁷⁰ M. Umer, R. W. Bomantara, and J. Gong, *J. Phys.: Mater.* **4**, 045003 (2021).
- ⁷¹ M. Umer, R. W. Bomantara, and J. Gong, *Phys. Rev. B* **103**, 094309 (2021).
- ⁷² J. H. Shirley, *Phys. Rev.* **138**, B979 (1965).
- ⁷³ T. Morimoto, H. C. Po, and A. Vishwanath, *Phys. Rev. B* **95**, 195155 (2017).
- ⁷⁴ T. Kitagawa, E. Berg, M. Rudner, and E. Demler, *Phys. Rev. B* **82**, 235114 (2010).
- ⁷⁵ T. Oka and H. Aoki, *Phys. Rev. B* **79**, 081406R (2009).
- ⁷⁶ G. Zhenghao, H. A. Fertig, D. P. Arovas, and A. Auerbach, *Phys. Rev. Lett.* **107**, 216601 (2011).
- ⁷⁷ N. H. Lindner, G. Refael, and V. Galitski, *Nat. Phys.* **7**, 490 (2011).

- ⁷⁸ M. S. Rudner, N. H. Lindner, E. Berg, and M. Levin, Phys. Rev. X **3**, 031005 (2013).
- ⁷⁹ M. C. Rechtsman, J. M. Zeuner, Y. Plotnik, Y. Lumer, D. Podolsky, F. Dreisow, S. Nolte, M. Segev, and A. Szameit, Nature **496**, 196 (2013).
- ⁸⁰ M. Claassen, H. -C. Jiang, B. Moritz, and T. P. Devereaux, Nat. Comm. **8**, 1192 (2017).
- ⁸¹ S. Kitamura, T. Oka, and H. Aoki, Phys. Rev. B **96**, 014406 (2017).
- ⁸² M. Hasan, D. Yudin, I. Iorsh, O. Eriksson, and I. Sheikhykh1, Phys. Rev. B **96**, 205127 (2017).
- ⁸³ M. Nakagawa, R. -J. Slager, S. Higashikawa, and T. Oka, Phys. Rev. B **101**, 075108 (2020).
- ⁸⁴ E. S. Mananga and T. Charpentier, J. Chem. Phys. **135**, 044109 (2011).
- ⁸⁵ E. S. Mananga and T. Charpentier, Phys. Rep. **609**, 1 (2016).
- ⁸⁶ T. Haga, Phys. Rev. E **100**, 062138 (2019).
- ⁸⁷ P. J. Lin-Chung, Phys. Rev. **88**, 1272 (1969).
- ⁸⁸ H. Okamoto, J. Phase Equilibrium **13**, 155 (1992).
- ⁸⁹ K. Sierański, J. Szatkowski, and J. Misiewicz, Phys. Rev. B **50**, 7331 (1994).
- ⁹⁰ J. R. Botha, G. J. Scriven, J. A. A. Engelbrecht, and A. W. R. Leitch, J. App. Phys. **86**, 5614 (1999).
- ⁹¹ M. Neupane, S. Xu, R. Sankar, N. Alidoust, G. Bian, C. Liu, I. Belopolski, T. Chang, H. Jeng, H. Lin, A. Bansil, F. Chou, and M. Z. Hasan, Nat. Commun. **5**, 3786 (2014).
- ⁹² Z. Liu, J. Jiang, B. Zhou, Z. Wang, Y. Zhang, H. Weng, D. Prabhakaran, S. Mo, H. Peng, P. Dudin, T. Kim, M. Hoesch, Z. Fang⁵, X. Dai, Z. X. Shen, D. L. Feng, Z. Hussain, and Y. L. Chen, Nat. Mater. **13**, 677 (2014).
- ⁹³ I. Crassee, R. Sankar, W. -L. Lee, A. Akrap, and M. Orlita, Phys. Rev. Materials **2**, 120302 (2018).
- ⁹⁴ L. Allen, S. M. Barnett, and M. J. Padgett, Optical Angular Momentum (CRC Press, 2003) Secs. 1.3 and 2.1.
- ⁹⁵ S. H. Autler and C. H. Townes, Phys. Rev. **100**, 703 (1955).
- ⁹⁶ P. L. Knight and P. W. Milonni, Phys. Rep. **66**, 21 (1980).
- ⁹⁷ E. J. Sie, J. W. McIver, Y. -H. Lee, L. Fu, J. Kong, and N. Gedik, Nat. Mat. **14**, 290 (2015).
- ⁹⁸ P. S. Pershan, J. P. van der Ziel, and L. D. Malmstrom, Phys. Rev. **143**, 574 (1966).
- ⁹⁹ A. V. Kimel, A. Kirilyuk, P. A. Usachev, R. V. Pisarev, A. M. Balbashov, and Th. Rasing, Nature **435**, 655 (2005).
- ¹⁰⁰ R. Hertel, J. Magn. Magn. Mater. **303**, L1 (2006).
- ¹⁰¹ H. -L. Zhang, Y. -Z. Wang, X. -J. Chen, J. Magn. Magn. Mater. **321**, L73 (2009).
- ¹⁰² M. Battiato, G. Barbalinardo, and P. M. Oppeneer, Phys. Rev. B **89**, 014413 (2014).
- ¹⁰³ E. O. Kane, J. Phys. Chem. Solids **1**, 249 (1957).
- ¹⁰⁴ J. M. Luttinger, Phys. Rev. **102**, 1030 (1956).
- ¹⁰⁵ In the present tetragonal structure of Zn_3As_2 , $d_1(\mathbf{k})$ and $d_2(\mathbf{k})$ have the leading-order terms of the form $ak_z(k_x + ik_y)^2$ with a as a constant. Here, one keeps contributions in $\mathcal{H}(\mathbf{k})$ up to the second-order terms with respect to \mathbf{k} by assuming that the higher-order terms can be neglected; consult also Ref. 8. This differs from the case of the body-centered tetragonal structure, in which there are second-ordered terms in $d_1(\mathbf{k})$ and $d_2(\mathbf{k})$.
- ¹⁰⁶ The interaction of light with electron between Wannier states $|b\mathbf{R}\rangle$ and $|b'\mathbf{R}'\rangle$ is given by $H'_{b\mathbf{R},b'\mathbf{R}'}(t) = \langle b\mathbf{R}|\mathbf{F}(t) \cdot \mathbf{r}|b'\mathbf{R}'\rangle = \mathbf{F}(t) \cdot \mathbf{R}\delta_{bb'}\delta_{\mathbf{R}\mathbf{R}'} + \mathbf{F}(t) \cdot \langle b\mathbf{R}|\mathbf{X}|b'\mathbf{R}'\rangle\delta_{bb'}\delta_{\mathbf{R}\mathbf{R}'} + \mathbf{F}(t) \cdot \langle b\mathbf{R}|\mathbf{X}|b'\mathbf{R}'\rangle\delta_{\mathbf{R}\mathbf{R}'}$, with $b(b')$, $\mathbf{R}(\mathbf{R}')$, and \mathbf{r} as a band index, a lattice position, and an electron position, respectively, and $\mathbf{X} \equiv \mathbf{r} - \mathbf{R}$. The third term of the second equality representing a dipole matrix element at different lattice position can be neglected because of the localization property of Wannier functions. By transforming this Hamiltonian from the lattice representation into a momentum representation, the first term in the second equality is eliminated from it as the Peierls phase, and the second term corresponds to an interband electric dipole interaction. For more detailed derivation, consult Supplementary Note 1 included in Supplementary Information of Ref. 65.
- ¹⁰⁷ J. Kerr, Philosophical Magazine **3**, 321 (1877).
- ¹⁰⁸ P. Weinberger, Philosophical Magazine Letters **88**, 897 (2008).
- ¹⁰⁹ T. Haider, International Journal of Electromagnetics and Applications **7**, 17 (2017).
- ¹¹⁰ U. Fano, Phys. Rev. **124**, 1866 (1961).